

CHAPTER 3

THE DESIGN OF THE INTERFEROMETER

“A whole is that which has beginning, middle and end.”
Aristotle

3.1 OPTICAL DESIGN OF THE INTERFEROMETER

3.1.1 Description of the interferometer

The optical design of the interferometer is shown in schematic form in figure 3.1. Details of the components may be found in Appendix A with results of optical testing in Appendix B. Appendix E contains details of the electronics equipment rack connections. Apart from the addition of path-folding mirrors, the design is that of a Twyman-Green interferometer. The collimator focal length is 1.5 m, the de-collimation length is 1.0 m. The overall size of the interferometer is approximately 1.2 x 2.4 x 0.3 m. The optical axis is 120 mm above the baseplate and the reference and measurement beams have a diameter of approximately 80 mm. Figure 3.2 shows the components of the interferometer with a perspective view of the optical layout in figure 3.3 with further details in figure 3.25.

The light sources for the interferometer are 3 frequency-stabilised helium-neon lasers operating at wavelengths of approximately 633 nm (red), 543 nm (green), and 612 nm (orange). The output of each laser is focused into a single mode optical fibre of 2.8 - 3.6 μm core diameter. The 3 fibres have their other ends terminated in a small ferrule and form a 3 spot light source. The small diameter of the fibre has two advantages: it decreases the effective angular diameter of the source at the collimator lens (see § 4.1.3) and it allows only one mode to propagate in the fibre, preventing the formation of large-scale speckle in the interference pattern [1]. The 3-fibre light source can also be used as an alignment aid when setting up the interferometer (see § 4.1.2.3).

The light exits the fibres and diverges with an angular spread which is dependent on the numerical aperture of the fibres, which is 0.12. The divergent beam from each fibre over-fills the collimator lens (diameter 100 mm) which subtends a numerical aperture of 0.03 at the source. The ends of the fibres are positioned at the focal point of the collimator lens, so the beam emerges from the lens fully collimated.

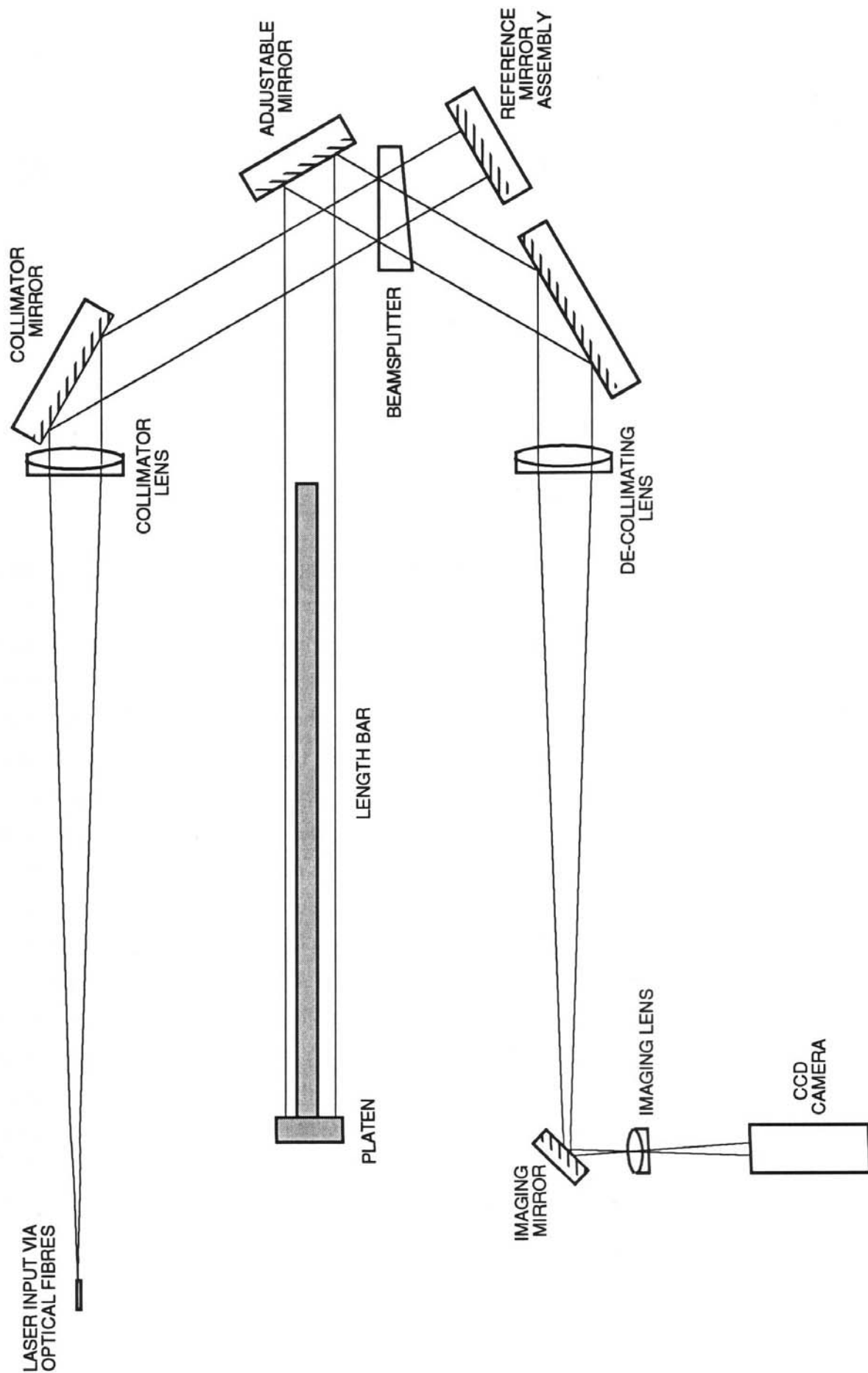


Figure 3.1 - Schematic design of interferometer optics

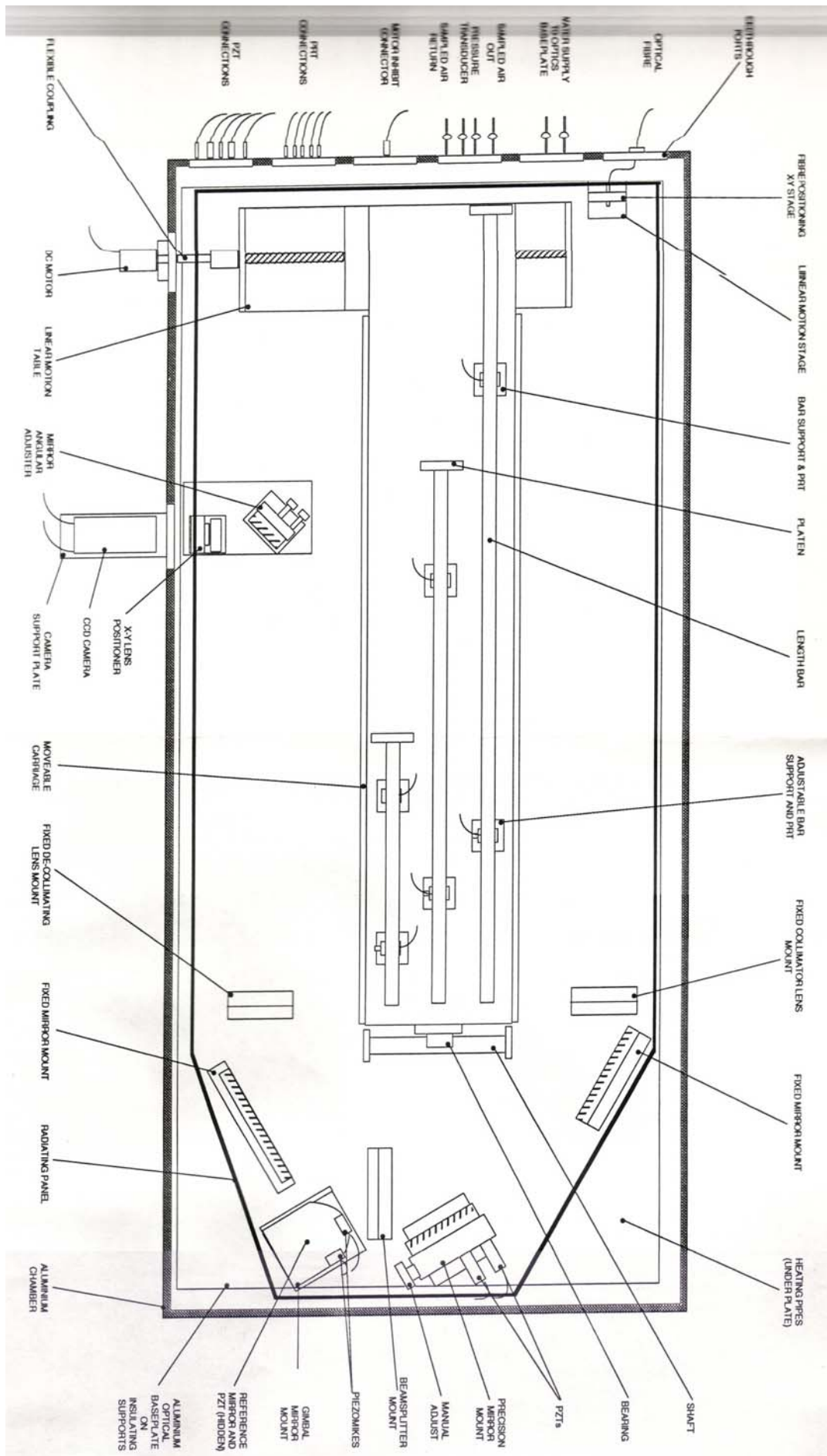


Figure 3.2 - Diagram showing the opto-mechanical components of the interferometer

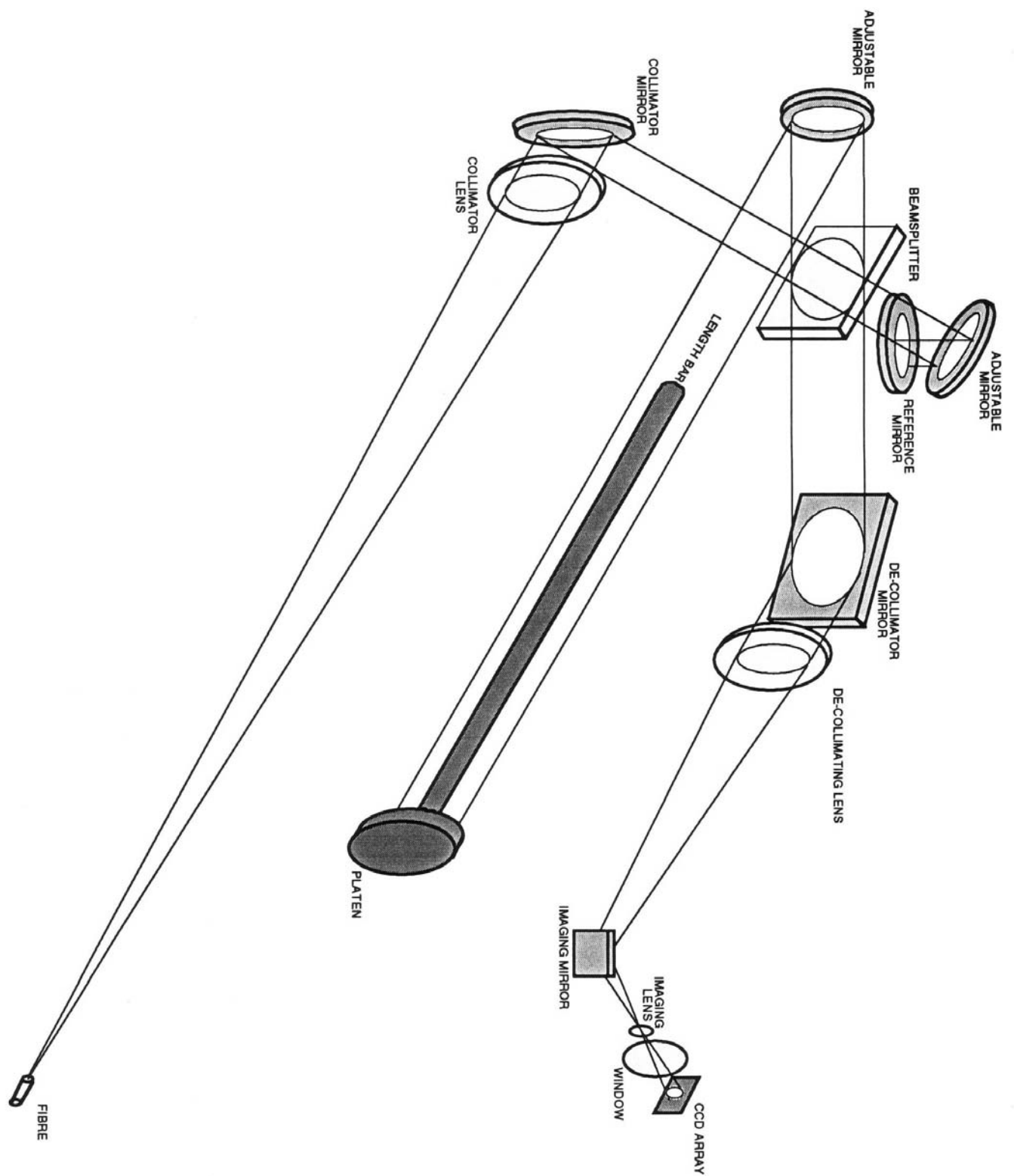


Figure 3.3 - Perspective view of optical components and directions of beams

Proper focusing of the collimator can be checked using either a shearing plate interferometer (see § 4.1.4) or by using an optical flat to re-direct the beam back to the source and then adjusting the focus until the spot size is a minimum. The focal length of the collimator was chosen to be 1.5 m for two reasons. Firstly, the larger the collimation length, the smaller the obliquity effect due to the size and positioning error of the source (see § 4.1.3) and secondly there was a commercially available achromatic doublet of focal length 1.5 m, suitable for the instrument (see optical testing in Appendix B).

The collimated beam is directed by a 150 mm diameter mirror (hereafter called the ‘collimator mirror’) onto the beamsplitter. The beamsplitter is coated for a nominal 50/50 transmission/reflectance and is wedged at 0.5° along its major axis to prevent secondary reflections from interfering with the primary transmitted and reflected beams.

The beam transmitted by the beamsplitter is the reference beam and is directed by a mirror angled at 45° (not shown in figure 3.1 for clarity) onto the reference mirror. The reference mirror actually lies in a horizontal plane, *i.e.* with its primary face horizontal. This face is coated with chromium which has a similar reflectivity (see Appendix A) to the measurement faces of length bars. In this way the contrast of the fringes is maximised since the reference beam and measurement beam have equal intensities.

The beam reflected by the beamsplitter is directed onto the length bar and platen by a remotely-adjustable mirror. Part of this measurement beam is reflected from the front surface of the bar and part by the platen surface.

The measurement and reference beams re-combine at the beamsplitter and are directed via two mirrors, a de-collimating lens and an imaging lens onto a CCD camera. The interference fringes formed by the interaction of the reference and measurement beams are located at infinity once they have emerged from the de-collimating lens and are imaged onto the CCD array by the imaging lens. This lens is also used to focus the image of the end of the length bar onto the CCD array. The image viewed by the camera is thus a superposition of the interference fringes, the image of the bar, and the partially out of focus image of the platen surface.

3.1.2 The interferometer chamber

Because the accuracy of the interferometer is dependent on knowing accurately the refractive index of the air in the measurement beam and because accurate fringe fraction measurements require stable fringes (and no air turbulence), the entire

interferometer (except for heat sources such as the camera and lasers) was constructed inside a sealed, aluminium-walled chamber. This ensures that the refractive index inside the interferometer is uniform and relatively stable and not affected by possible external contaminants such as exhaled water vapour and CO₂ or vapour from solvents such as acetone or alcohol used for cleaning bars and platens.

An alternative would have been to measure the bars in a vacuum. This idea was rejected for two reasons. Firstly, the length of a metal bar is shorter when in vacuum compared to in air due to the absence of air pressure compressing it. For example, a 1 m bar would shorten by approximately 20 nm under vacuum conditions compared to normal atmospheric pressure. The exact magnitude of the shortening would depend on material properties of the bar, such as the exact value of Young's modulus. Without accurate determination of these properties, especially the transition from un-hardened to hardened material near the end faces, the exact change in length of the bar could not be calculated, and hence the length of the bar at 1 atmosphere would not be known. Secondly, the absence of any conductive or convective medium in the chamber would lead to an increase in the thermal soaking time required for the bars to reach thermal equilibrium at each temperature. Thus the use of a vacuum system was rejected in favour of a sealed chamber at atmospheric pressure.

The pressure inside the chamber varies slowly (the chamber is not pressure-sealed) with external atmospheric pressure variations. A totally sealed chamber was considered, but this would have required a substantial stainless steel construction which would have had safety implications. The chamber is temperature-controlled (see Chapter 8) further reducing variations in refractive index. (For the effect of these variations on refractive index, see § 7.3).

The chamber is a 3 unit construction and consists of the optical table surface, a 'collar', and a lid. The optical table has a surface of non-magnetic 300-series stainless steel, with sealed tapped holes and a specially lapped area for sealing against a silicon seal on the bottom face of the collar. The thermal expansivity of the steel is $16.6 \times 10^{-6} \text{ K}^{-1}$. The collar is made of welded aluminium, 16 mm thick, 350 mm high. The collar encloses an area of 2250 x 1050 mm. On one side of the collar there are 6 feed-through ports for connecting equipment inside the chamber to the outside world, together with 2 ports on a long side wall for rotary drive to the translation table and a window for the output beam.

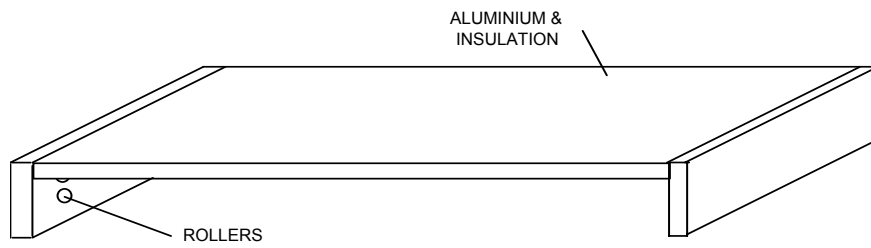


Figure 3.4 - Lid of chamber

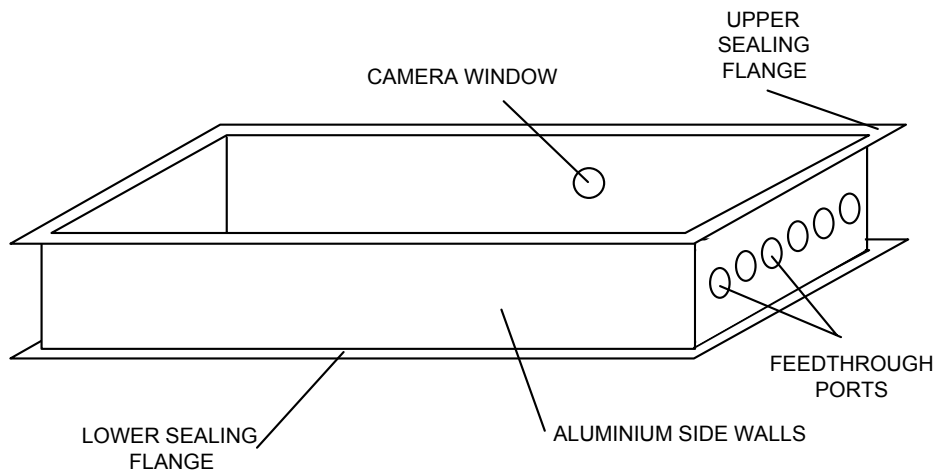


Figure 3.5 - Aluminium 'collar' used as side walls of chamber

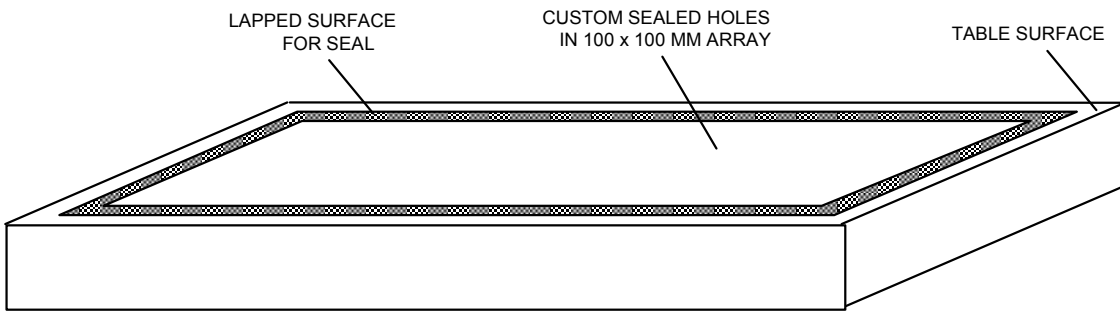


Figure 3.6 - Optical table used as base of interferometer chamber

Further details of the heating and insulation of the interferometer chamber can be found in chapter 8.

3.2 DETAILS OF INTERFEROMETER COMPONENTS

Figure 3.2 (fold-out) shows a plan of the interferometer showing most of the components. Technical specifications and dimensions of the optical and opto-mechanical components can be found in Appendix A. Some of the components and systems have been specially designed for the interferometer and are detailed below.

3.2.1 Design of lasers used with the interferometer

Because the use of the single mode lasers is vital to the interferometer, the design of the lasers will be examined, starting with the background theory of the operation of the helium-neon gas laser.

3.2.1.1 Helium-neon laser theory

The continuous wave helium-neon (He-Ne) gas laser contains a mixture of approximately 8 parts of helium to 1 part of neon at a total pressure of a few millibars. The laser consists of an optical cavity, similar to that of a Fabry Perot etalon, formed by

a plasma tube with optical quality mirrors at the ends. The gas in the tube is excited by a high voltage discharge of approximately 1.5 to 2.5 kV, at a current of approximately 5 to 6 mA. The discharge creates a plasma in the tube which emits radiation at various wavelengths corresponding to the multitude of allowed transitions in the helium and neon atoms.

The coherent radiation emitted by the He-Ne laser at approximately 632.8 nm corresponds to the $3s_2 - 2p_4$ transition in neon. The excited $3s_2$ level is pumped by energetic $2s_1$ helium atoms colliding with the neon atoms; the $2s_1$ helium energy level is similar in energy to the $3s_2$ level of neon and the lighter helium atoms are easily excited into the $2s_1$ level by the plasma discharge (see figure 3.7). The excess energy of the collision is approximately equal to kT , *i.e.* it is easily removed by the atoms in the plasma as kinetic (thermal) energy.

The collisional pumping of the $3s_2$ level in neon produces the selective excitation or population inversion which is required for lasing action. The $2p$ neon state decays in 10^{-8} second to the $1s$ state, maintaining the population inversion. The $1s$ state relaxes to the ground state by collision with the walls of the plasma tube. The laser gain is quite small and so losses at the end mirrors must be minimised by using a high reflectance coating, typically 99.9%. The output power is limited by the fact that the upper lasing state reaches saturation at quite low discharge powers, whereas the lower state increases its population more slowly. After a certain discharge power is reached, further increase in the power leads to a decrease in the population inversion, and hence lower light-power output.

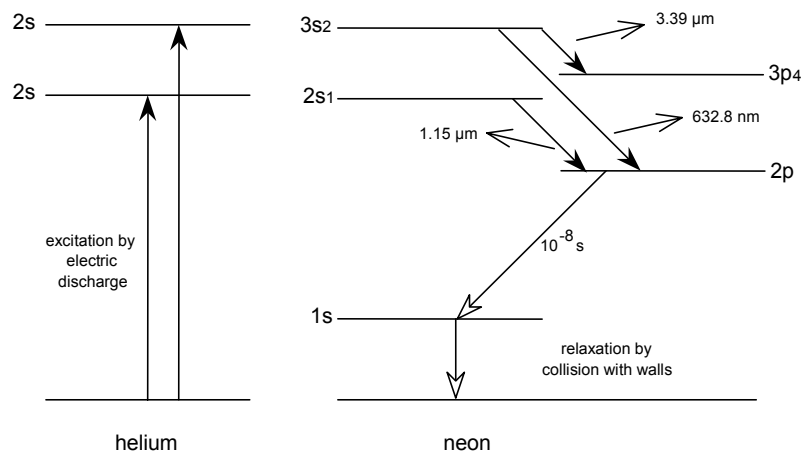


Figure 3.7 - Energy levels in the He-Ne gas laser for 632.8 nm radiation

The 632.8 nm (approximate) operating wavelength is selected by the spacing of the end mirrors, *i.e.* by the total length of the optical cavity, l_c . The length of the cavity must be such that waves reflected by the two end mirrors are in phase. The wavelengths of successive axial modes are then given by

$$2l_c = m\lambda \quad (3.1)$$

These modes are separated in wavenumber by

$$\Delta\sigma = \frac{1}{2l_c} \quad (3.2)$$

or in terms of frequency

$$\Delta\nu = \frac{c}{2l_c} \quad (3.3)$$

This would lead to a series of narrow lines of similar intensity in the spectrum, if it were not for the effects of Doppler broadening and the gaussian distribution of atoms available for stimulated emission. The availability of atoms for stimulated emission is given by

$$A(\sigma) = \frac{1}{a\sqrt{\pi}} e^{-\frac{\sigma^2}{a^2}} \quad (3.4)$$

where

$$a^2 = \frac{2kT\sigma_0^2}{Mc^2} \quad (3.5)$$

k is Boltzman's constant, T is the temperature of the gas, M is the molecular weight of the gas, and σ_0 is the line centre. This distribution has a half width at $w_\sigma = 2a\sqrt{\ln 2}$.

Also, when a particular mode is oscillating, there is a selective depopulation of atoms with specific velocities (laser cooling) which leads to a dip in the gain profile. For modes oscillating away from the centre of the gain curve the atomic populations for the two opposite directions of propagation are different due to the equal but opposite velocities. For modes oscillating at the centre of the gain curve, the two populations become a single population of effectively stationary atoms. Thus a dip in the gain profile occurs at the centre of the gain curve - the so called "Lamb dip". Some early laser stabilisation schemes locked to the Lamb dip [2] but the position of the dip is dependent on other parameters of the laser such as the position of the gain curve and so is unstable.

For early lasers with a typical cavity length of 1 m the mode spacing was 0.5 m^{-1} , with a gain profile width of approximately 5.5 m^{-1} . Thus several axial modes were present in the gain profile with gains sufficient for laser action, and so two or more modes would operate simultaneously, making the laser unsuitable for interferometry. By using a shorter tube and then carefully lowering the power of the discharge and hence lowering the gain curve, it was possible to achieve single mode operation.

Having selected a single mode, the fundamental limitation to the linewidth (and thus to the temporal coherence) is spontaneous noise fluctuations which broaden the line into a Lorentzian function [3]

$$w_{\sigma} = \frac{8\pi h c^2 \sigma w_c^2}{P} \quad (3.6)$$

or

$$\Delta \nu = \frac{\pi h \nu}{P} (\Delta \nu_c)^2 \quad (3.7)$$

where P is the operating power of the laser, h is Planck's constant, c is the speed of light and w_c is the linewidth due to the cavity. However a more common-place limitation is the thermal vibration of the tube size which directly affects the wavelength of the oscillating mode. For the lowest frequency stretching mode of the laser tube

$$w_{\sigma} = \sigma \sqrt{\frac{2kTV}{E}} \quad (3.8)$$

where V is the volume of the tube material of Young's modulus E .

3.2.1.2 Single mode laser wavelength stabilisation schemes

To allow a laser to be used in interferometry with coherence lengths above a few millimetres it must operate in a single mode. There have been many proposed schemes for laser stabilisation [4].

As mentioned above, the Lamb dip was used in an early stabilisation scheme. Here the intensity of the output beam was monitored as the length of the cavity was modulated, for example by Piezo Electric Transducers (PZTs). Another scheme used mirrors external to the laser cavity which were modulated, with the output intensity being monitored and the laser locked to the centre of the Lamb dip [5]. The reproducibility of lasers locked to the Lamb dip is limited by the shift of the Lamb dip centre as the pressure of the gas inside the laser tube varies and also by a discharge current dependent shift. The large width of the Lamb dip itself (about 5×10^{-7} of the laser frequency) also limits the frequency stability obtainable from this technique.

Use has also been made of tuneable Fabry-Perot etalons in a similar system. Other groups have locked the output of one laser to the frequency of a second stabilised laser. Others have used neon discharge absorption cells [6] where the laser was locked to the absorption spectrum of neon in an external tube, the theory being that the un-excited neon would have a narrower linewidth than the neon in the laser discharge.

3.2.1.3 Laser frequency-stabilisation using saturated absorption

The technique with the greatest stability is used in the Primary Reference lasers which represent the UK's Primary Length Standard and involves controlling the length of the cavity to alter the wavelength and locking the wavelength to an absorption line in saturated iodine vapour [7,8,9]. This is a more stable technique since the absorption takes place from a thermally populated energy level which is free from the perturbing effects of the electric discharge in the laser tube.

If the output beam from a laser is passed straight through an absorption cell, then absorption takes place over a Doppler broadened transition. However if the cell is placed in a standing wave optical field then the high intensity laser field saturates the absorption and a narrow dip appears at the centre of the absorption line corresponding to molecules which are stationary or moving perpendicular to the direction of the beam. This dip produces an increase in the laser power in the region of the absorption line. This increase can be detected and the laser frequency stabilised to the centre of the absorption line. The absorption line is reproducible and insensitive to perturbations. The line width is dependent on the absorber pressure, laser power and energy level lifetime. Saturated absorption linewidths are typically less than 1×10^{-8} of the laser frequency.

An evacuated quartz cell containing a small iodine crystal is placed in the laser cavity and temperature controlled to 23 °C. The laser mirrors are mounted on PZTs and the end plates are separated by invar bars to ensure a thermally stable cavity. A small frequency modulation is applied to the laser via one of the PZTs. This leads to an amplitude modulation in the output power which is detected using a phase sensitive detector and fed back to the other PZT as a correction signal. The frequency control system employs a photodiode, low noise amplifier, coherent filter and phase sensitive detector followed by an integrating filter.

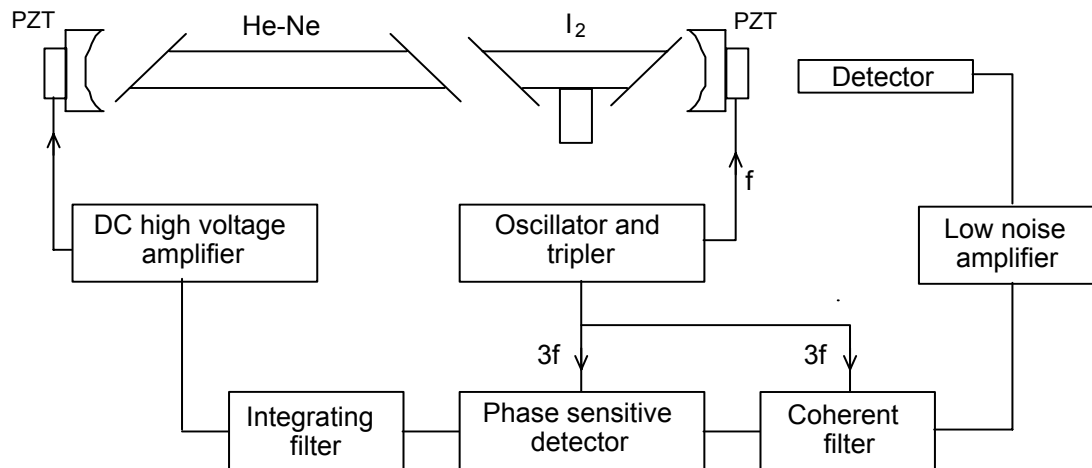


Figure 3.8 - Schematic diagram of an iodine-stabilised He-Ne laser

Detection of the absorption signal at the laser modulation frequency results in a first derivative scan which shows the hyperfine components superimposed on the sloping background of the neon gain curve. The laser may be servo-locked to any of these lines, the frequency of which has been fixed internationally at the time of the re-definition of the metre in 1983 in terms of the speed of light [10] (see § 1.3.5).

Iodine-stabilised He-Ne lasers can achieve frequency stability [11] of a few parts in 10^{13} over a period of a few minutes with long term reproducibility of a few parts in 10^{11} .

3.2.1.4 Zeeman-Stabilised 633 nm Lasers

An alternative technique to saturated absorption is used in the commercial lasers used in the Primary Length Bar Interferometer. The method of stabilisation used for these lasers is based on the Zeeman effect [12,13,14]. A longitudinal magnetic field is applied to a single mode He-Ne laser tube, splitting the normally linearly polarised mode into two circularly polarised modes which are oppositely polarised. A field strength of 0.02 T is sufficient to split the modes, which remain locked together at low B-field, to produce the linear polarisation. These two modes differ in frequency by 300 kHz, around a mean frequency corresponding to the original linear mode [15].

The wavelength difference between the two modes is due to each of the two modes experiencing a different refractive index and therefore different optical path length, in

the He-Ne mixture. This arises due to magnetic splitting of an atomic state of neon, shown in figure 3.9.

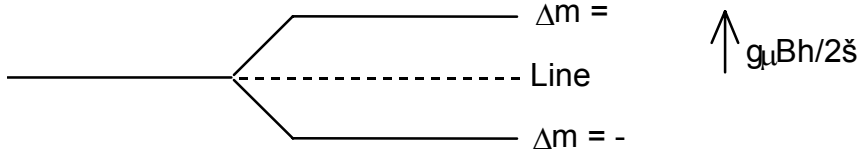


Figure 3.9 - Magnetic splitting of neon - g is the Landé g factor, μ the Bohr magneton, B the field strength, and h is Planck's constant

The $\Delta m = +1$ mode couples with the left polarised mode and the $\Delta m = -1$ mode couples with the right polarised mode. The relative frequencies of the polarisation modes are given by

$$\omega_{\pm} = \frac{cN}{2Ln_{\pm}} \quad (3.9)$$

where c is the speed of light, L is the cavity length, n_{\pm} the refractive index for the mode, and N the axial quantum number [16]. The shape of the refractivities ($n_{\pm} - 1$) of the two components and their difference is shown in the following figure.

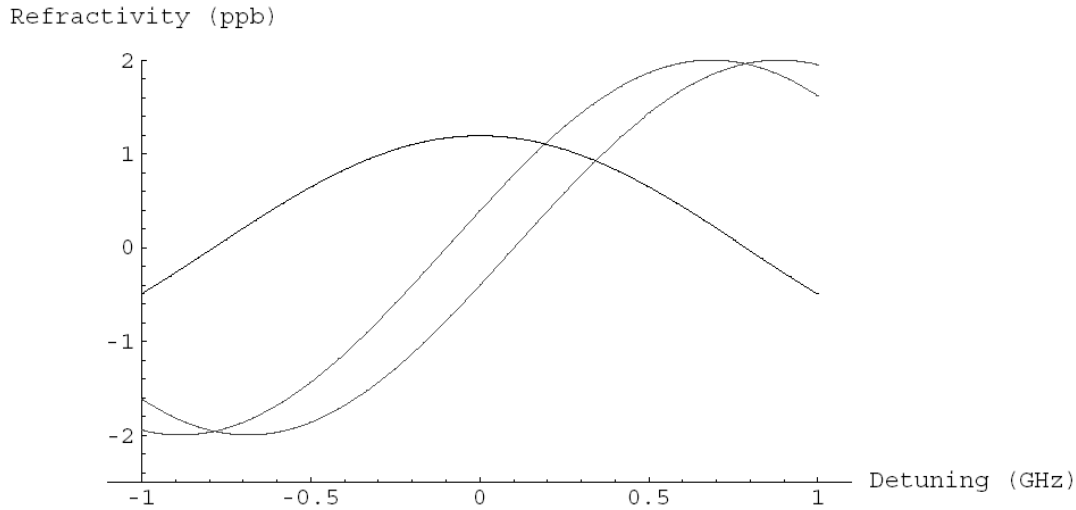


Figure 3.10 - Refractivities of two Zeeman modes in 632.8 nm laser mode: darker line is difference between the two refractivities depicted by the two lighter curves

Note: the exact shape of the difference near ω_0 depends on the strength of the Zeeman splitting and the amount of saturation.

The important feature of the Zeeman split gain curve is that the position of ω_0 does not vary with B field strength - it remains at the original (un-split) line centre, and is thus a

very stable lock point. If one combines the 2 oppositely polarised components, one observes the beat frequency between them.

from
$$\omega_{\pm} = \frac{cN}{2Ln_{\pm}}$$

$$\Delta\omega = \omega_{+} - \omega_{-} = \frac{cN}{2L} \left(\frac{1}{n_{+}} - \frac{1}{n_{-}} \right) \quad (3.10)$$

which is proportional to $\omega_0 [\chi_{+}(\nu) - \chi_{-}(\nu)]$

where $c_{+}(n)$ and $c_{-}(n)$ are dispersion functions for the left and right polarised modes, respectively. For a more complete derivation see Tomlinson *et al* [17]. As the laser is tuned by altering the cavity length L , the beat frequency will pass through a peak which corresponds to the laser frequency being tuned to ω_0 .

This tuning curve can be used as an error signal for controlling the laser frequency. The particular method chosen to modulate the laser cavity length is thermal expansion. A thin foil heater is attached to the laser tube, connected to a square-root power amplifier. Two magnets are fixed onto the tube to provide the axial magnetic field. A polarising beamsplitter is used, together with a photodetector and amplifier to detect the ~ 300 kHz beat frequency. This error signal is fed to various stages of counters and amplifiers and then to the heater.

The laser tube requires a period of approximately 10 minutes to reach the correct temperature corresponding to the required tube length for operation at frequency ω_0 . A phase-locked loop circuit then fine-tunes the temperature and length of the cavity, to stabilise the laser at the correct frequency. This last process takes only a few seconds to achieve lock. The frequency stability of the laser is 5×10^{-10} for 1 s averages and is white-noise limited for averaging times between 100 ms and 10 min. The day to day resettability of the laser frequency is typically $\pm 5 \times 10^{-10}$. There is also a linear drift of frequency with the amount of time for which the laser has operated. This is due to clean up of the helium-neon mixture, whilst undergoing discharge. The rate of drift is unique to each laser, but is stable with respect to time, and can be ascertained after a few calibrations of the laser frequency. As an example, Sasagawa [18] showed drift rates of 0.3 to 5.7 ± 0.5 MHz per calendar year, though these were for frequency against date, rather than against operational time. Rowley [16] reported a drift rate of -1×10^{-11} per hour of operation.

The operation of the green (543 nm) and orange (612 nm) lasers are roughly similar, although some of the electronic techniques used are different. The frequency stability of the green and orange lasers is similar to that of the red, though the short term fluctuations of the orange laser are larger than those of either the red or green lasers.

3.2.1.5 Calibration of the Zeeman-stabilised 633 nm laser

The calibration of the laser is achieved by launching the light from the Zeeman stabilised laser into a multi-mode optical fibre, which terminates near to the iodine stabilised laser in a different laboratory. The beam combines with that from the Primary laser via a beamsplitter. The beat signal between the two frequencies is measured with a photodetector.

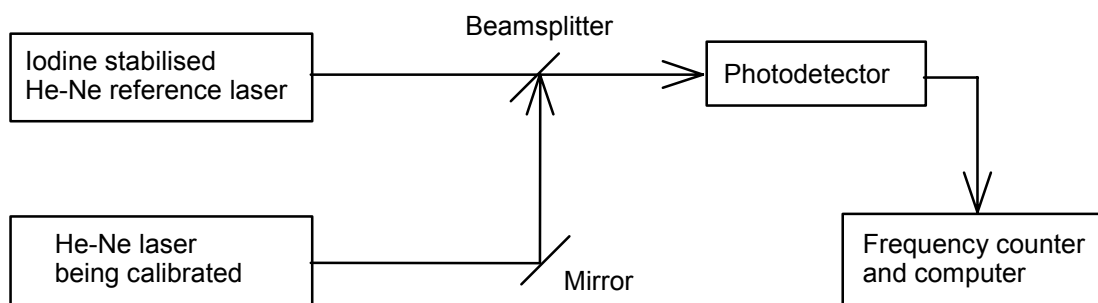


Figure 3.11 - Calibration scheme for Zeeman stabilised laser

This beat frequency is easy to detect, and to monitor via a computer, over a number of hours. A typical value of the beat signal is 260 MHz, with the iodine standard (g component) at approximately 473 612 345 MHz.

The Zeeman laser emits two polarisations (the 2 Zeeman components) which are separated by 0.5 MHz. The 2 components are present in the beam at the interferometer which thus measures with a wavelength which is the mean of these two components. During the laser calibration, beats between each of these frequencies and the iodine frequency are observed. The mean of these is deemed to be the calibrated wavelength of the Zeeman laser.

The Zeeman-stabilised laser incorporates a modulation signal, which is applied to the heaters to achieve the lock point. This signal is a square wave, of frequency 3-5 Hz. This causes a periodic contraction and expansion of the laser tube, and thus the frequency (and wavelength) of the red laser undergoes a sinusoidal modulation. The depth of this modulation is 7 MHz peak to peak, and is approximately 70° out of phase with the square wave modulation signal.

The heater signal is inverted and is used as a synchronisation signal for the timing of the phase stepping digitisation. Thus it is important to calibrate the laser at the synchronisation point, which occurs at the rising edge of the inverted (TTL level) signal (falling edge of the heater signal).

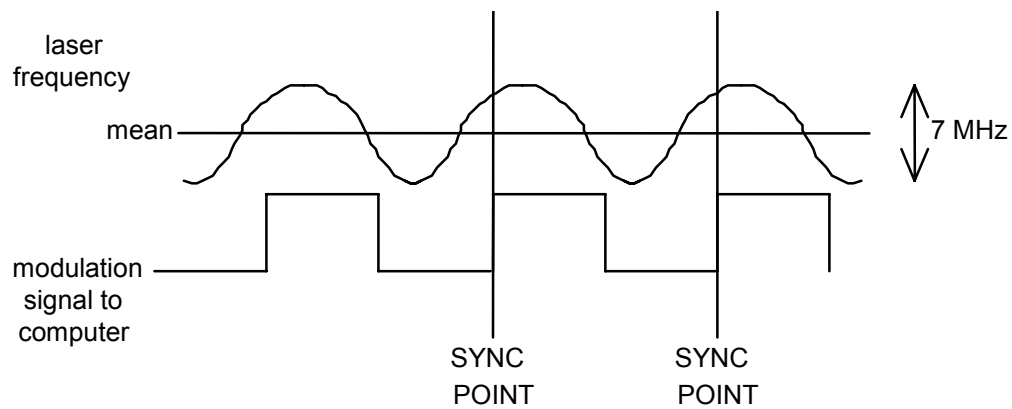


Figure 3.12 - Synchronisation diagram for red Zeeman stabilised laser

By using a frequency to voltage converter, it is possible to synchronise the frequency determination to the correct edge in the modulation signal.

As an example, a red laser, serial number U5, was calibrated after 4103 hrs of use. The mean frequency of the laser was found to be 473 612 605 MHz, and the correction for the modulation signal was +3 MHz, making the effective frequency 473 612 608 MHz, and the vacuum wavelength 632.990 872 57 nm.

3.2.1.6 Calibration of 612 nm and 543 nm lasers

The orange (612 nm) and green (543 nm) lasers are also calibrated by beat frequency comparison with iodine-stabilised reference lasers. There is no modulation signal and hence no correction for these lasers. The 612 nm reference laser is also an internationally accepted realisation of the metre (see Table 1.3). The 543 nm laser is currently being proposed (at the CCDM) as an additional realisation.

3.2.2 The optical fibre illumination delivery system

The lasers are sources of heat and are thus mounted away from the interferometer. The output beam of each laser, after passing through the acousto-optic modulator, is focused using a pair of lenses into the core of a single mode optical fibre.

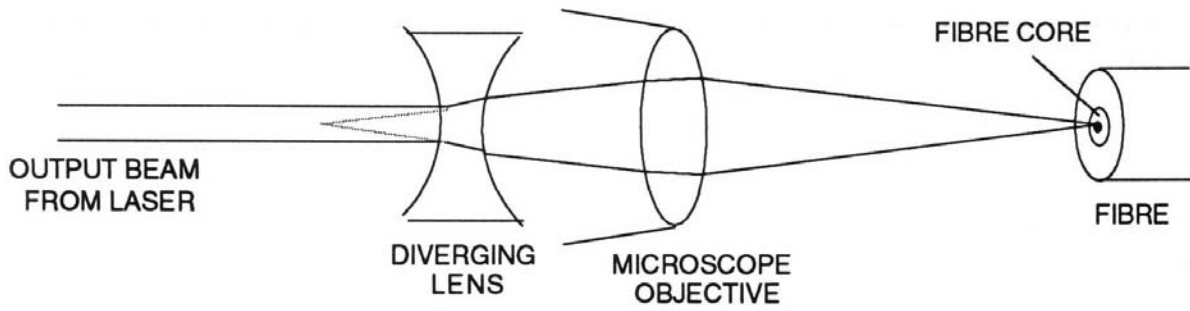


Figure 3.13 - Focusing of laser beam into fibre core

From Fourier-diffraction theory, the size of the focal spot is dependent on the numerical aperture of the input beam. The diverging lens is required to decrease the size of the focused spot so that it fits within the 3 - 4 μm diameter of the fibre core. This increases the energy coupling between the beam and the fibre core. The coupling efficiency is also dependent on beam-fibre geometry and the surface form and finish of the fibre. With good quality fibre surfaces the limiting factor is the aberration induced by the diverging lens. To keep the dimensions of the coupling optics small, the power of the lens is relatively high, this leads to higher aberrations and lower coupling efficiency. With longer focal lengths [19] it is possible to increase the efficiency of the coupling to approximately 80% compared to the 20% efficiency obtained with the optics used. Typical coupling efficiency was measured using an optical power meter.

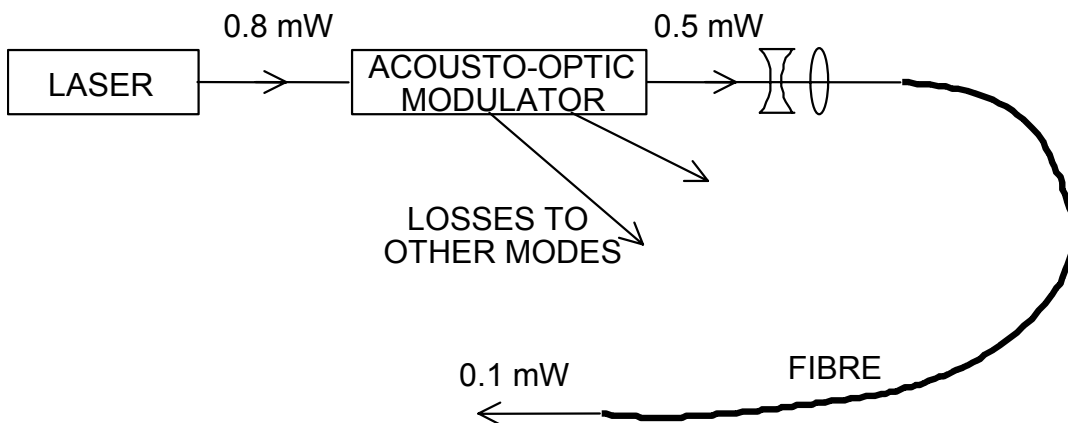


Figure 3.14 - Coupling efficiency of fibre launch

Fortunately 20% coupling efficiency is sufficient for the interferometer. Higher power in the collimator would result in the camera's automatic gain control operating.

Single mode fibres are not as easy to handle or launch light into as multi-mode fibres, however they support only one transmission mode. This prevents the formation of

large-scale speckle in the image which can be a problem unless use is made of electronic speckle interferometry (ESPI) algorithms. Various systems of speckle removal have been tried [20,21]. These rely on mixing the modes, *e.g.* by shaking the fibre or shining through a rotating round glass screen, such that over the averaging period of the detector, the image appears uniform.

For the interferometer it was necessary to have a small diameter source with a relatively small numerical aperture (NA). Most multi-mode fibres have core diameters of 50 μm and greater, and usually relatively large NAs (0.3). Single mode fibres operating in the visible spectrum have approximately 4 μm diameter cores, and small NAs (0.12), making them ideal. The chosen fibres have a core diameters of 2.8 and 3.6 μm and an NA of 0.12.

Each laser beam is focused into one single mode fibre. It is common to couple multiple sources into a single fibre by using spliced fibre couplers.

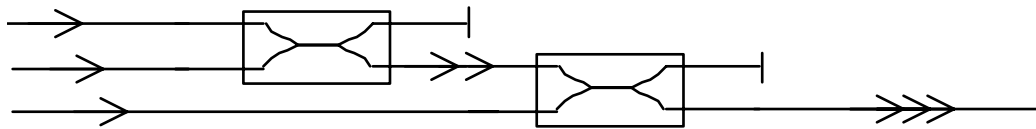


Figure 3.15 - Three source coupling using 2:2 couplers

With common 2:2 couplers a proportion of the input energy is lost via the unused port. Even with 2:1 couplers there are losses in the forwards direction and splitting of the reverse beam decreases the power available for detection when aligning the interferometer (see § 4.1.2.3).

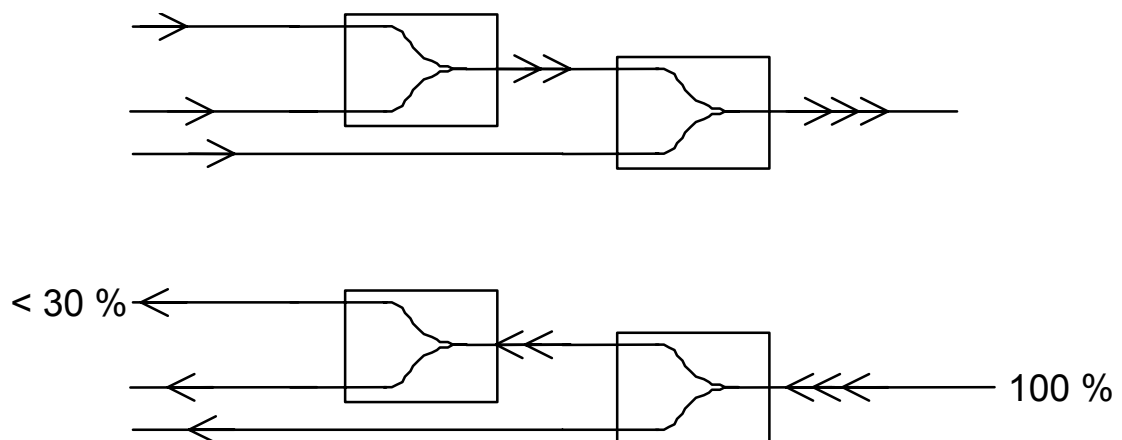


Figure 3.16 - Three source coupling and return spot detection using 2:1 couplers

3:1 couplers can also be used, though these are generally custom-made, expensive and prone to losses, especially single mode devices.

The solution adopted for the NPLBI is to simply use 3 separate fibres and join them mechanically at their output ends [22]. The 3 fibres have the outer buffer coating removed, leaving the 3 - 4 μm core and the 80 - 125 μm primary cladding. The 3 stripped fibres are cemented into a 6 mm diameter ferrule to form a 3-spot light source. Each source thus has an effective diameter of 3 - 4 μm with the sources separated by approximately 100 μm . The emerging beam diverges from each fibre at an angle of 7° , determined by the numerical aperture of the fibre. Thus at the collimator lens, 1.5 m away from the fibres, the beam has expanded to a diameter of over 200 mm, overfilling the 100 mm diameter collimator lens. The lens is thus illuminated approximately uniformly by the central gaussian peak of the beam.

Two different fibres are used in the 3-spot system, a 3M EOTEC FS-SN-3221 for the 633 nm and 612 nm wavelengths, and a 3M EOTEC FS-VS-2211 for the 543 nm wavelength, however in practice there is very little loss whichever fibre is used for each wavelength, and the 3 wavelengths are similar enough to prevent multiple mode operation in any of the fibres.

3.2.3 Reference mirror assembly

The reference mirror assembly consists of a mirror mounted at 45° to the vertical and the reference mirror mounted on a PZT translator. The mounts are attached to a rigid side panel for stability (not shown in figure 3.17).

The PZT is a commercial design digital piezo translator (DPT) (Queensgate Instruments AX100) incorporating a capacitance micrometer at the head of the PZT. PZTs can be prone to various problems during movement. These include hysteresis, non-linearity, and drift with time [23]. These errors can cause errors in the phase-retrieval due to improper phase-stepping [24]. The usual method of overcoming these problems is to use a self-calibration check of the PZT's performance before each measurement is made [25]. This is time consuming and does not always guarantee adequate performance. Alternatively, other phase calculation algorithms can be chosen which are less sensitive to phase-stepping errors [26].

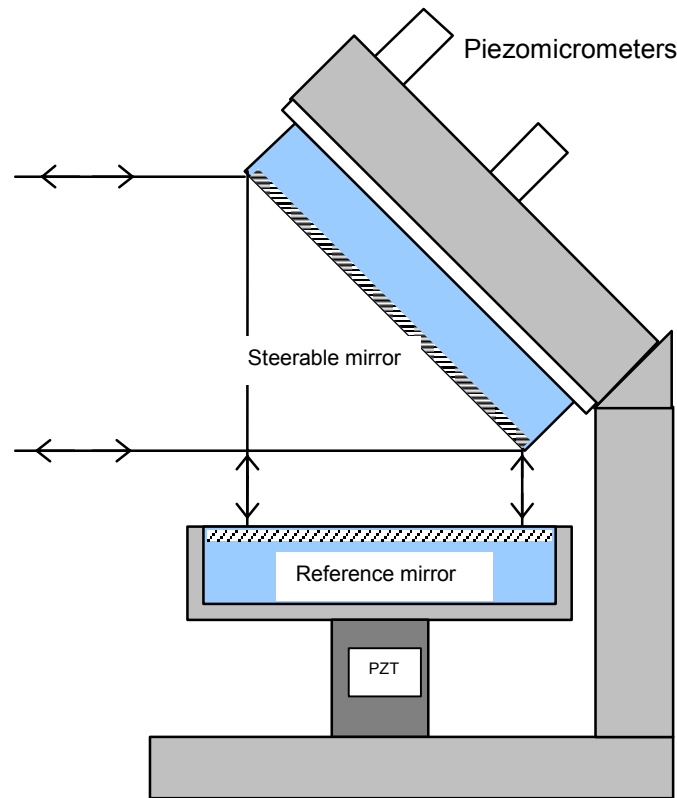


Figure 3.17 - Reference mirror assembly

The commercial DPT system used in the Length Bar Interferometer overcomes the above problems by using a capacitive sensor [27] mounted in the DPT case which responds linearly to elongation of the PZT. The signal from this sensor is used in a feedback loop to correct for any inaccuracies in the DPT movement. The position sensor has picometre sensitivity and the system as a whole has a noise level less than 1 nm RMS (0.003 fringe at $\lambda = 633$ nm).

The DPT case is made of ZERODUR™ (a low thermal expansion coefficient glass) and INVARTM to minimise temporal and thermal drift. The whole DPT system is microprocessor controlled allowing digital control of the movement of the DPT, with readout of position attained. Once the readout and the movement of the DPT have been initially calibrated, there is no need to re-calibrate before each measurement, and over the four years that this device has been operating, there has been no noticeable drift in the DPT calibration, *i.e.* the digital phase step size used in the phase-stepping has not been altered from its initial value.

The AX100 positioning controller is addressed by the computer via an IEEE-488 interface. Using a simple set of instructions the mirror can be positioned at any of 16384 points along its operating range. The range is controlled by the resistance of a precision resistor in the input to a summing amplifier which sums positional control

signals from the IEEE interface, an external voltage input, and the front panel potentiometer.

The step size of the DPT system was calibrated by digitising interference fringe intensity at a single point whilst repeatedly stepping the DPT in single steps. The step size was calculated to be 1.066 nm. When performing the phase stepping, the mirror must move in steps of 1/4 fringe ($\lambda/8$) - this corresponds to DPT steps of sizes 74, 63 and 72 for the 633 nm, 543 nm and 612 nm wavelengths respectively.

The angled mirror is adjusted by 2 piezo-micrometers (Physik Instrumente P854.00 Piezomikes). These allow a manual adjustment of 6 mm and fine, remote adjustment using a PZT with 30 μm range. Other designs of mounting the reference mirror were tried, with the mirror mounted vertically, *i.e.* with the PZT stepping the mirror horizontally. These designs used springs or counterweights to try to constrain the mirror. With all these designs it was not possible to prevent tilting of the mirror during phase-stepping, which resulted in a linear variation of phase-step angle down the image, and hence errors in the calculated phase-maps. Since an angled mirror was necessary in the reference arm for steering purposes, it was a simple solution to mount this mirror at 45° and direct the beam downwards onto the reference mirror.

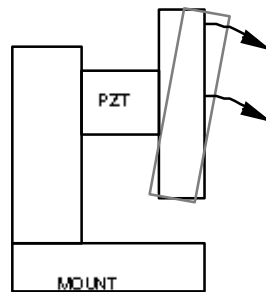


Figure 3.18 - Exaggerated tilting of reference mirror when translating horizontally

3.2.4 Design of the imaging optics

Ignoring path-folding mirrors, the imaging optics of the interferometer are shown in schematic form in figure 3.19. Because the collimator lens is properly focused on the source, the optics in the interferometer are telecentric. A small achromat is used at the focal plane of the de-collimating lens to focus the image of the end of the bar onto the CCD.

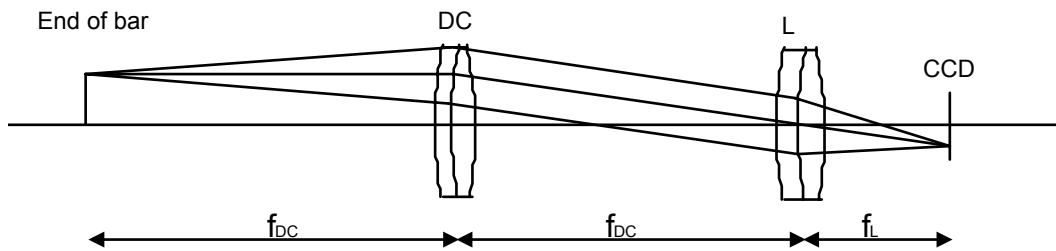


Figure 3.19 - The imaging optics of the NPLBI

Because the Twyman-Green interferometer uses a collimated light source, the source image rays are parallel to the length bar. This means that the images of the end of the bar and the partially out of focus image of the platen will have the same scale in the CCD image plane.

The system of imaging optics is a compromise. There are 2 surfaces of interest in the measurement beam: the exposed face of the bar and the surface of the platen. These are separated spatially by up to 1.5 m (or 3.0 m path difference). Although the use of a small source increases the focal depth of both the fringe and object imaging optics, it is still necessary to focus at some point in the object path.

For consistency, the plane that was imaged out of the interferometer was chosen to be the front (un-wrung) face of the bar. Bars positioned in the interferometer are thus placed such that their front faces are in the focal plane of the de-collimating lens. It is the end surface of the bar rather than the platen which is of particular interest for flatness measurements. The surface of the reference flat is effectively smoothed by software to a best fit surface. The imaging system also allows easy adjustment to cope with rectangular long series gauge blocks, which are also measured in the interferometer.

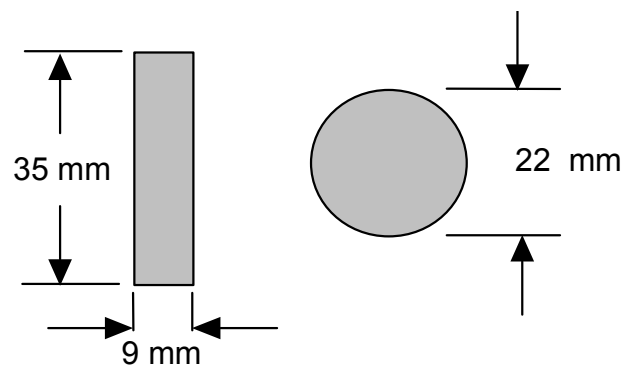


Figure 3.20 - Comparison of end face sizes of length bars and long series gauge blocks

Because long series gauge blocks have to be measured resting on their narrow edge, a different magnification is required to fit the gauge block in the image field. This is achieved by replacing the imaging lens with one of different focal length and re-positioning the camera (two mechanical stops mark the camera positions for gauge blocks and length bars).

Thus the length bar (or gauge block) and platen are both imaged, with the interference fringes, although there is slight degradation of the image at the edge of the bar due to diffraction of the beams at grazing incidence along the bar. This is particularly evident for long bars and necessitates a software ‘mask’ at the edge of the bar in the phase calculations.

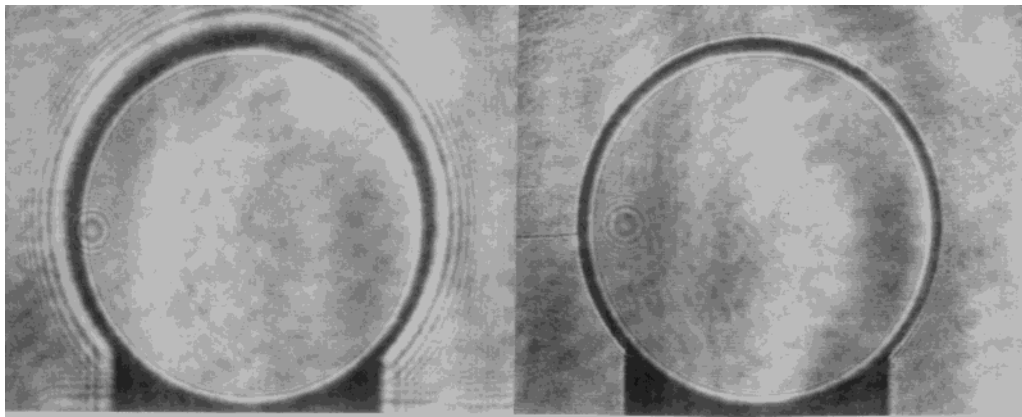


Figure 3.21 - Video prints of images of a 1000 mm length bar (left) and a 225 mm length bar (right) with fringes suppressed, showing different diffraction effects at the edge of the bars due to the different lengths

3.2.5 Design of length bar supports

Due to flexing of length bars under their own weight and the weight of any wrung-on platen, it is conventional to support them at two points along their length in such a way that the end faces remain parallel and vertical - for un-wrung bars these points are called the ‘Airy points’. For bars with platens wrung to one face, the supports points are moved further out, towards the ends of the bar to compensate for the weight of the platen - a full derivation is given in Appendix C.

It is important that there are no further forces acting on the bar other than its weight and the reactions at the two supports otherwise further bending will occur. This prevents attachment of platinum resistance thermometers (PRTs) to measure the bar temperature at points other than the support points. Special supports were designed to include PRTs in such a way that the bar was freely supported at the supports, whilst remaining in good thermal contact with the PRTs.

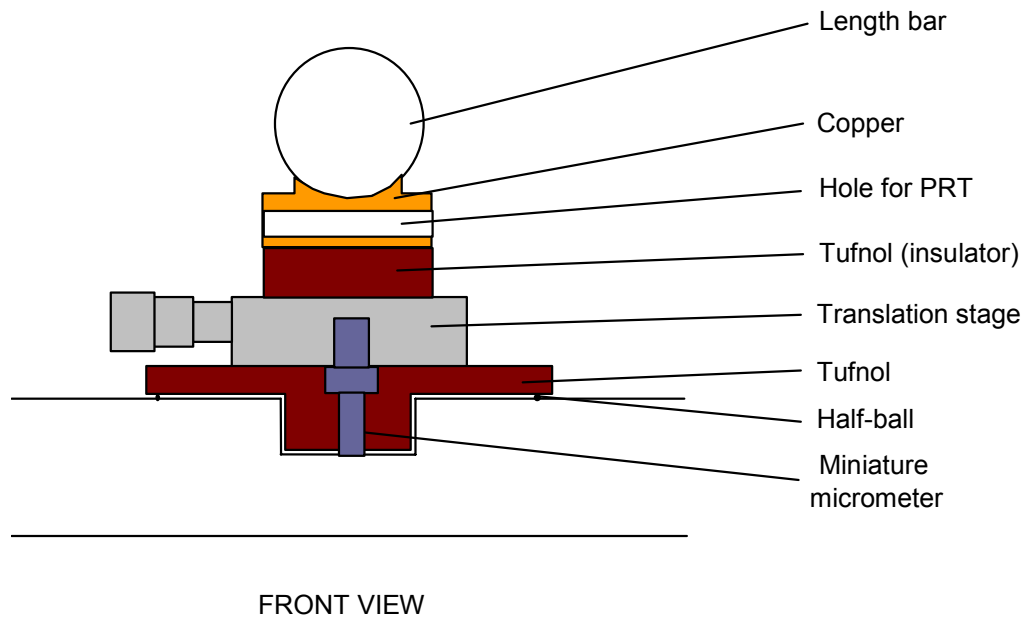


Figure 3.22 - Length bar supports with integral PRTs, end view

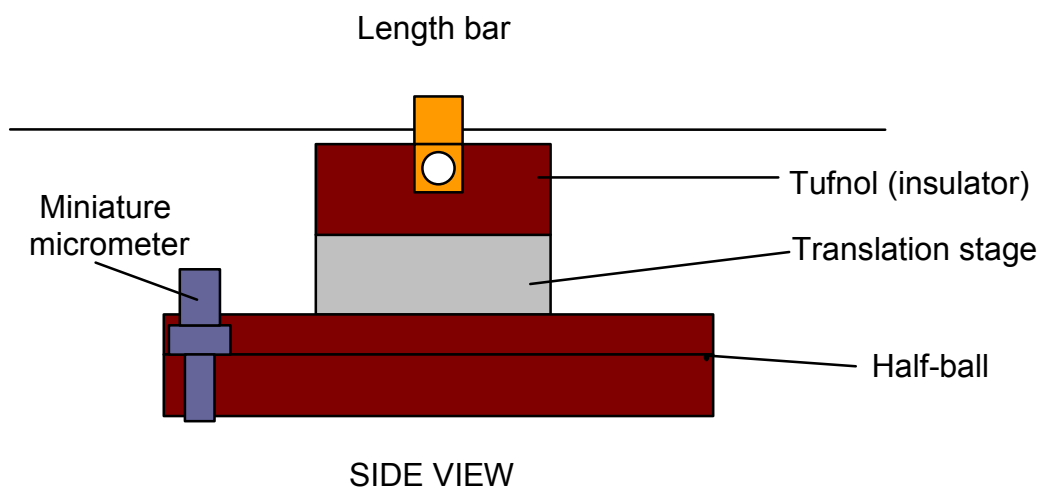


Figure 3.23 - Length bar supports with integral PRTs, side view

Each support consists of a small copper block (chosen for good thermal conductivity), shaped to fit the underside of the length bar or gauge block, with a hole into which a PRT is placed. The copper blocks are fitted tightly into insulating spacer blocks made from TUFNOL™. The supports used at the front end of the bars also contain miniature micrometers and translation stages. These are used to position each bar in the interferometer so that it lies parallel to the measurement beam axis, to within the range of adjustment of the PZT-adjustable mirror. The two PRTs inside the copper blocks are in good thermal contact with the length bar, and hence the temperature of the bar can be measured simply as the mean temperature of these PRTs, assuming any temperature gradients in the bar are small or linear (see § 8.4.1).

The insulating supports are mounted at three vertical-contacting points onto the carriage using three half-balls, one in the slot and two on the top surface. In the case of the adjustable supports, the miniature micrometer takes the place of one of the balls.

3.2.6 Length bar support carriage design

In order to allow more than one bar to be sealed inside the chamber at one time, a translatable carriage was designed to accept up to 3 length bars or gauge blocks. The carriage is made from a block of PERALUMAN (see appendix A) of size 1.5 x 0.26 x 0.02 m with stiffening members attached underneath and at the sides. This forms a solid base for the length bar supports. Three slots were milled into the carriage, 90 mm apart, to a depth of 8 mm, with a mutual flatness and parallelism of 0.5 mm. The length bar (or gauge block) supports fit into these slots and can be positioned at any length along the carriage to cope with bars of different lengths.

The carriage is mounted on a translation stage via a strip hinge. The motion is thus driven from one end via rigid strip which allows the carriage to tilt about only one axis. The other end of the carriage is supported on a bearing which traverses a shaft. The carriage has to be more constrained than a conventional kinematic mount because it must undergo one dimensional translation whilst the bars remain parallel to the measurement beam. If the system is considered as three points in space, corresponding to the bearing and two points at the opposite corners of the strip hinge, then the hinge effectively fixes the x, y and z co-ordinates of two points, and hence fixes rotation about 2 axes, and the bearing fixes y and z of the remaining point. This fixes rotation about the third spatial axis and allows only translation in x (when the x co-ordinates of the other two points translate similarly).

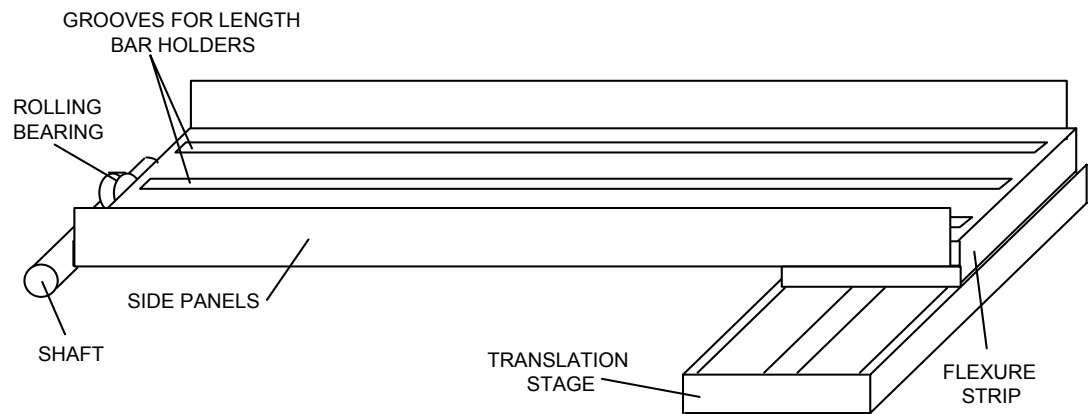


Figure 3.24 - Length bar support carriage

During translation, interference fringes visible in the image remain parallel with the same spacing whilst moving across the image. This indicates that there is no tilting of the carriage, which translates forwards slightly as well as sideways (the translation axis is not perfectly orthogonal to the measurement axis) - this is however no problem. The carriage and supports can be seen in figure 3.25 which shows a close-up view inside the chamber.



Figure 3.25 - View of carriage, supports, length bars and optics inside chamber

3.2.7 Design of the adjustable mirror in the measurement arm

Fine adjustment of the alignment of the measurement beam with the axis of the bar to be measured is achieved using a mirror mounted on a 2-directional flexure. The flexure is tilted by PZT control and is mounted in a commercial high-quality mirror mount for coarse, manual adjustment. The flexure can be tilted in two orthogonal directions about axes which pass through the centre of the flexure stage.

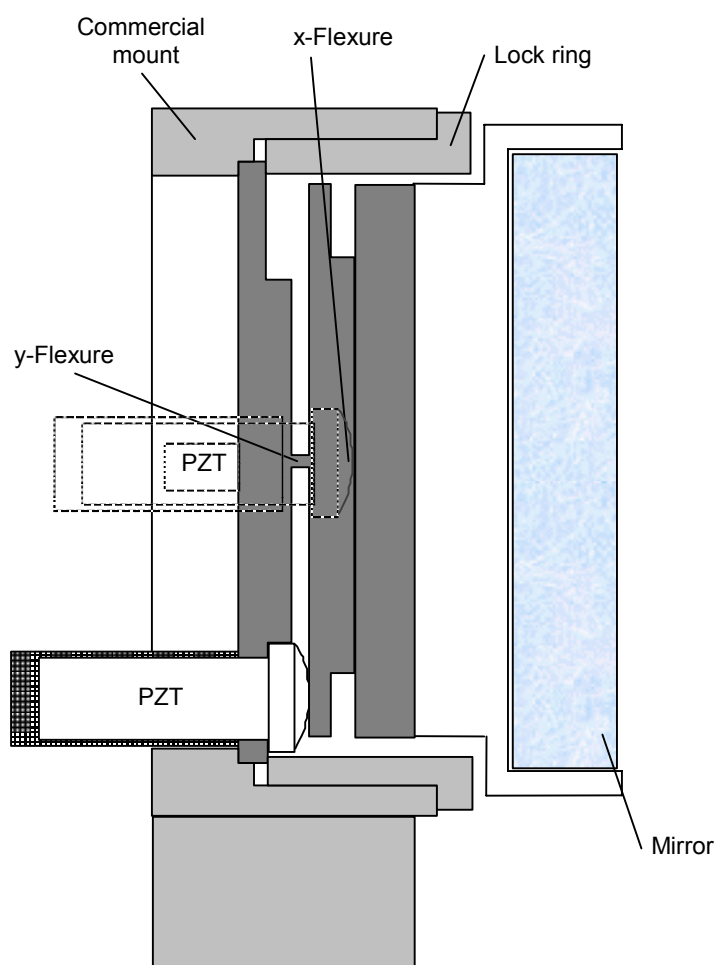


Figure 3.26 - Flexure system for tilting mirror

3.2.8 External equipment rack and computing equipment

The interferometer chamber is connected to an equipment rack which houses the electronic equipment used to perform measurements inside the interferometer. These units are: a Druck pressure transducer, a Michell hygrometer transducer & displays, a CO₂ meter and display, a Tinsley precision resistance bridge with 15 channel selector switch and standard resistor, PZT power supplies, a PTFE re-circulating sample pump,

the controller for the Queensgate AX100 DPI system, a power supply for the carriage motor, the CCD camera power supply and a residual current circuit breaker.

In turn, signals from the rack are routed to the control computer and display monitor. The signals are TTL level IO signals, IEEE bus, video signal and video genlock signal. The water temperature controller is connected with flexible PVC tubing to the lid and baseplate pipes.

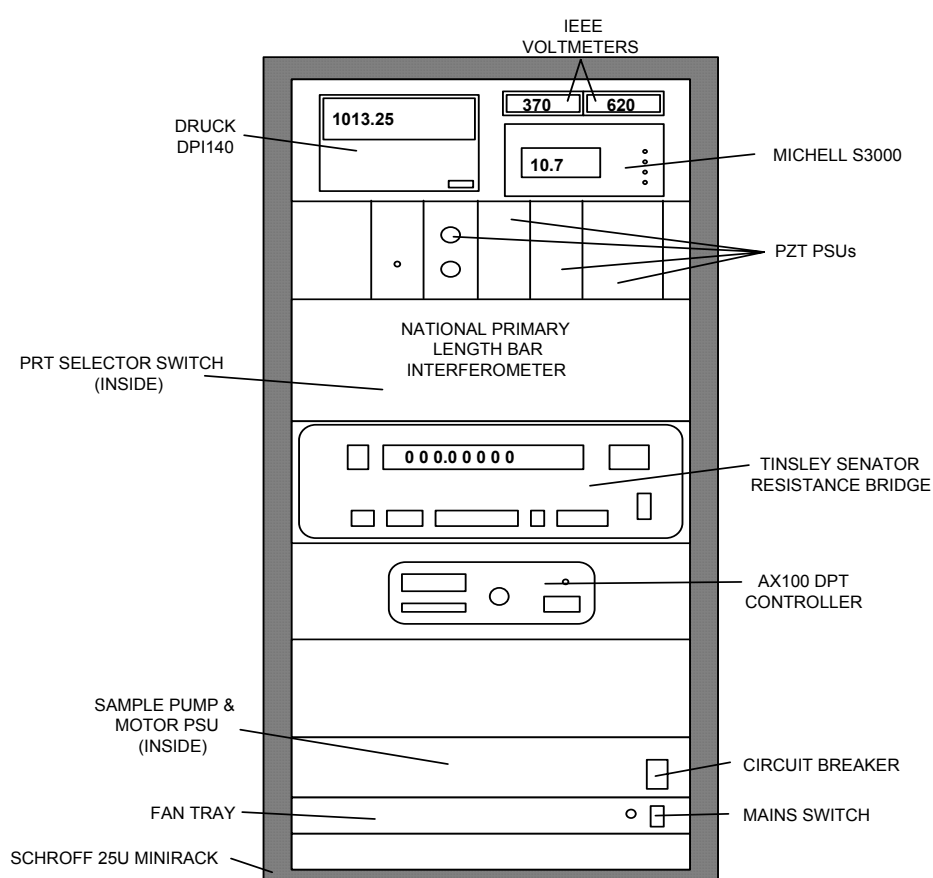


Figure 3.27 - Schematic front view of equipment rack

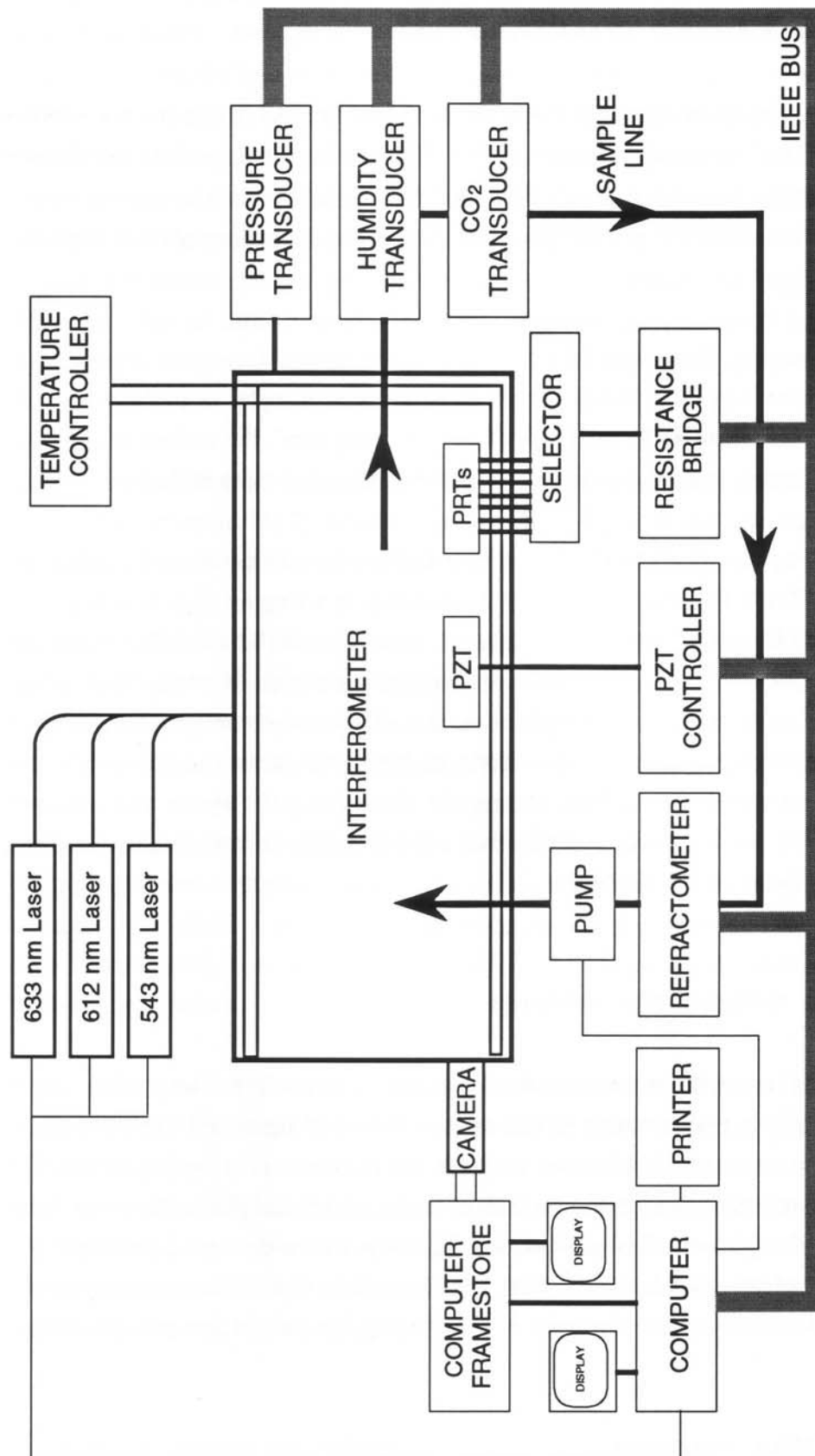


Figure 3.28 - Schematic diagram of interferometer & external equipment

3.3 DOUBLE-ENDED INTERFEROMETRY

This addition to the interferometer was not part of the original design but was conceived as an additional experimental technique to enhance the capabilities of the interferometer and to provide a useful research tool for future measurements concerned with the ‘wringing film’ thickness and the ‘phase correction’ (see definitions of these terms which follow).

When measuring the length of a bar wrung to a platen, the result obtained by an interferometer may be different to that obtained using a stylus or probing instrument because of four factors: the thickness of the ‘wringing film’, the surface roughness, the ‘phase correction’ and the geometrical form of the measuring faces of the bar.

By measuring the length of the bar without being wrung to a platen, the effect of the wringing film is removed and thus measurements of wringing film thickness can be attempted. There is a complication however in that there will be a different size phase correction since the beam will be reflecting off both ends of the bar rather than reflecting off one end of the bar and also the platen surface. A second advantage is that the double-ended system will allow measurements of both end faces simultaneously. With interferometry using wrung bars, one face is obscured by the platen, and any surface effects which would affect the parallelism measurements are averaged out by fitting a function to the surface of the platen.

3.3.1 The wringing film thickness

When being measured interferometrically according to BS 5317, a length bar should be measured with a platen wrung to one face as shown in figure 2.13 and described in § 2.5.1. The measured length then includes the thickness of a ‘wringing film’ - the molecular layer that separates the surfaces of the length bar and platen. However, in some situations a length bar will be used as an artefact, *e.g.* for validating the performance of a Coordinate Measuring Machine (CMM), where it will be used in the un-wrung state. For accurate measurements, the thickness of the wringing film should then be subtracted.

3.3.2 Surface roughness

The effect of the surface roughness of the platen and length bar surfaces depends on the size of the probe used to probe them. For a conventional mechanical probe (as used on

the NPL Length Bar Machine), the probe radius is typically 1-2 mm, thus the probe will contact the ‘peaks’ - the high points of the surfaces. For interferometry, the probe may be considered to be the light beam. In this case the effective size of the probe will be of the order of the wavelength of the light used: 543 - 633 nm. This will penetrate areas of the surface and will reflect from both the peaks and valleys, appearing on average to reflect from a surface mid-way between the peaks and valleys. BS 4311 (1993) for gauge blocks specifies that the platen should have a flatness of 0.025 μm (25 nm) over the measuring area - this is similar to the roughness expected of the gauge block and length bar surfaces. Thus the effect of surface roughness on interferometrically-measured length ought to cancel since the platen and length bar (or gauge block) should have similar surface roughnesses.

However, this is not the case, as the surface roughness of gauge blocks has been found to vary by approximately 20 nm within a single set of gauges [28]. Because length bars are made of a similar material, a similar variation is expected.

There are a number of techniques for the measurement of surface roughness [29,30] some of which NPL hopes to research in the next three years with a view to reducing the length measurement uncertainty due to surface roughness for gauge block and length bar calibrations. The most common technique used currently for measurement of surface roughness of gauge blocks uses an integrating sphere (Ulbricht’s sphere). In this technique, white light is reflected off a surface to be measured and by means of an integrating sphere with photoelectric detector, the ratio of the diffuse (R_d) to specularly-reflected light (R_s) is measured. It is assumed that the roughness of the test surface is proportional to the square-root of this ratio (R_d/R_s). This technique requires a calibrated surface, for reference.

Because the new interferometer does not yet have a means of measuring the surface roughness of the platen and length bar surfaces, the difference between the two values will lead to a length measurement error. Over the years 1989-1993, the overall correction applied to measurements of steel gauge blocks on steel platens at NPL has ranged from - 40 nm to + 15 nm, with the mean at - 14 nm. One can expect a similar, or larger value for measurements of length bars on platens. Thus a figure of -14 nm \pm 25 nm will be assumed for later uncertainty calculations.

3.3.3 Phase change on reflection

When light reflects at normal incidence off the surface of a dielectric of higher refractive index than the incident medium, there is a π radians phase shift on reflection

due to the continuity of the E-field at the boundary between the two media. If the reflecting medium is a non-dielectric, it has a complex refractive index and by solving the equations for the amplitude reflection coefficients at the surface it can be shown that there is a phase shift of between 0 and π radians, depending on the properties of the media. This is the case when the beam in the interferometer reflects off the surfaces of the bar and platen. It can be shown [31] that the phase shift, δ , is given by

$$\tan \delta = \frac{2n_1 k_2}{n_1^2 - n_2^2 - k_2^2} \quad (2.10)$$

where n_1 and n_2 are the refractive indices of the incident and reflective media respectively and k_2 is the extinction coefficient in the reflecting (semi-absorbing) medium.

From reference texts [32], typical values for these variables for steel are $n_2 = 2.4$, $k_2 = 3.4$ ($\pm 20\%$). For reflection in air, $n_1 = 1$, this gives a value $\delta = -23^\circ$ (or $180^\circ - 23^\circ = 157^\circ$). Thus the light beam appears to reflect off surfaces approximately 20 nm outside the gauge and platen surfaces, even if the surfaces are microscopically smooth. For a 20% variation in k_2 , δ varies by 5° , corresponding to a variation in measured length of 4.4 nm, for $\lambda = 633$ nm. This variation in k_2 is probably typical for the range of steels used for gauge blocks, length bars and platens. The worst possible difference in material properties could therefore give rise to a length measurement error of ± 8.8 nm.

Techniques for measuring the phase change on reflection range from multiple-reflection interferometry [33] comparing the phase shift on reference and test surfaces to the phase-stepping interferometer of Ishikawa *et al* [30] which used a coupled Twyman-Green-Fizeau interferometer. In this scheme, the ‘optical’ surface of the gauge block, corresponding to the mean surface from which the light is reflected and the surface of the flat, form a Fizeau interferometer. The Fizeau interferometer is one arm of a Twyman-Green interferometer. This design is used to measure the apparent position of the optical plane of the gauge block by phase-stepping the Twyman-Green interferometer to obtain information about the phase shift. Unfortunately, this technique assumes a zero wringing film thickness and zero surface roughness of the optical flat, which may not be the case.

The effects of the surface roughness and the phase change on reflection are often combined into one correction termed the ‘phase correction’.

3.3.4 Effect of surface form errors of measuring faces

In the interferometer, the length of the bar is measured as the perpendicular separation between the centre of the exposed measurement face and the surface of the platen wrung to the other end. This requires an interpolation from the phase data measured on the platen to the area covered by the bar. If the wrung measurement face of the bar is not flat, the interpolation will not accurately reflect the shape of the bar. If the other measuring face is flat, then when measured with the other face wrung, the length measurement will be different. However, both measurements are in accordance with the standard, which is why it is important to measure the flatness of the measuring faces of length bars (see § 6.5).

3.4 OTHER DOUBLE-ENDED DESIGNS

In the double-ended interferometer of Dorenwendt [34] the measurement beam of a Michelson interferometer is split and extended with additional mirrors, forming a triangularly closed path.

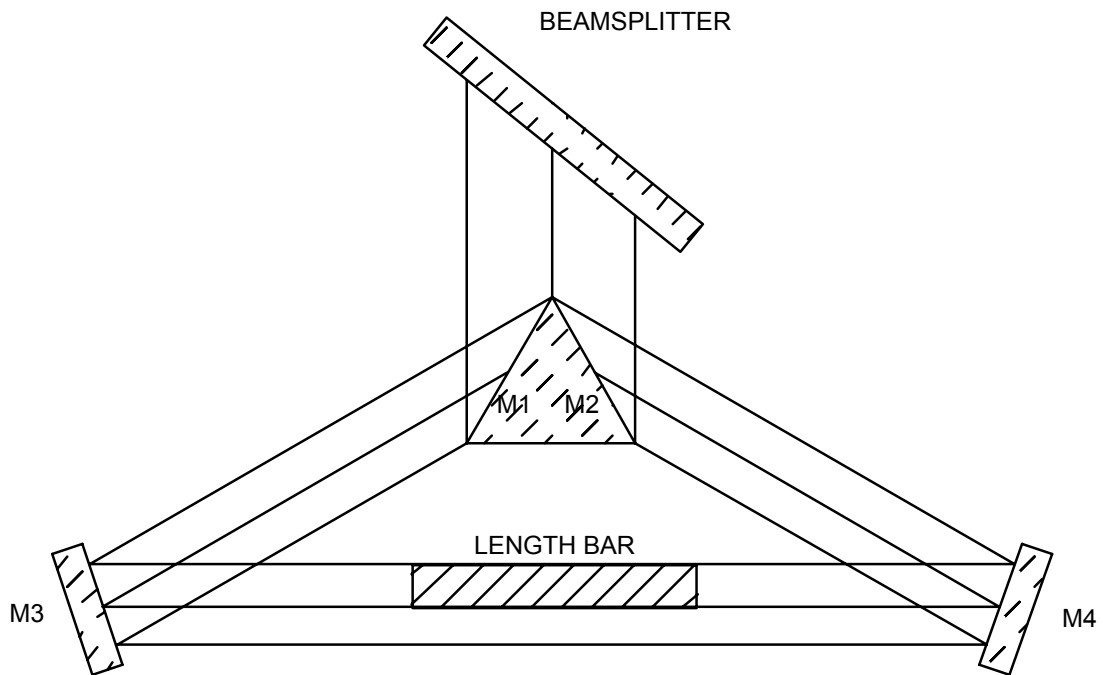


Figure 3.29 - Double-ended interferometer of Dorenwendt

In this design, four extra surfaces are introduced, increasing the complexity of the alignment and introducing further aberrations into the system. In the analysis of this interferometer, Dorenwendt arrived at two values which can be measured in the interferogram which he called ‘fictitious step heights’ L_1 and L_2

$$L_1 = \frac{L}{2} - a \quad L_2 = \frac{L}{2} + a \quad (3.11)$$

where L is the length of the bar and a is the deviation in the direction of measurement from the symmetrical position of the length bar in the optical path. Thus the sum of the two measured step heights represents the optical length of the bar in the un-wrung state.

Dorenwendt further stated that the effects of the phase change experienced by the light in reflecting from the extra mirrors will cancel, provided that the surface characteristics of the pairs of mirrors are similar. This will now be examined.

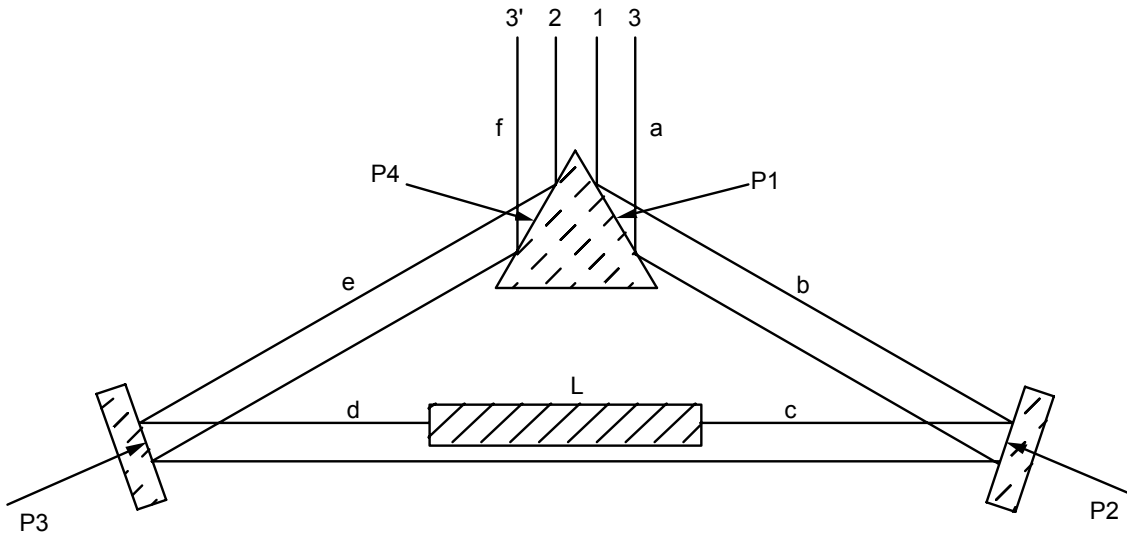


Figure 3.30 - Analysis of triangular interferometer of Dorenwendt

Let the optical path length of each of the three beams (right face, left face, reference) be given by ϕ .

$$\begin{aligned} \phi_1 &= 2(a + b + c + P_1 + P_2) \\ \phi_2 &= 2(f + e + d + P_3 + P_4) \\ \phi_3 &= (a + b + c) + (d + e + f) + L + (P_1 + P_2) + (P_3 + P_4) \end{aligned} \quad (3.12)$$

Now the measurable quantities in the image are the phase differences $\phi_3 - \phi_1$ and $\phi_3 - \phi_2$.

$$\begin{aligned} \phi_3 - \phi_1 &= L - (a + b + c) - (P_1 + P_2) + (d + e + f) + (P_3 + P_4) \\ \phi_3 - \phi_2 &= L + (a + b + c) + (P_1 + P_2) - (d + e + f) - (P_3 + P_4) \end{aligned} \quad (3.13)$$

Thus the sum of the two measured phase differences

$$(\phi_3 - \phi_1) + (\phi_3 - \phi_2) = 2L \quad (3.14)$$

From equations (3.13) the quantity $(a + b + c) + (P_1 + P_2) - (d + e + f) - (P_3 + P_4)$ can be identified as corresponding to $2a$ in equation (3.11).

Note that these equations do not require that $(P_1 + P_2) = (P_3 + P_4)$ unless it is desired that $a = 0$, for which $(a + b + c) = (d + e + f)$ *i.e.* the bar is in the symmetrical optical path position. Thus the effects of the surface properties of the additional mirrors on the phase change do not affect the overall length measurement. However aberrations of the mirrors will affect the wavefronts and could lead to an error in the measured length or the surface form of the bar.

3.5 DOUBLE-ENDED INTERFEROMETRY IN THE PRIMARY LENGTH BAR INTERFEROMETER

As part of the Primary Length Bar Interferometer a new double-ended interferometer has been designed and constructed. This design requires only one additional pair of mirrors which are used in the form of a pair of roof mirrors. The bar and carriage are displaced sideways and the roof-mirror system placed behind the bar. A different lens and camera position are selected because a different magnification is required to image both ends of the bar, compared to just one end. The roof-mirror arrangement is shown in figure 3.31.

In the image, there are 3 distinct regions: the front face of the bar, the rear face and the reference surface surrounding the bar. In this case, the reference surface corresponds to the surface of the beamsplitter since the beam travels around the bar twice, *i.e.* the image in the background area is the interference between the normal reference beam and a sheared version of the measurement beam. This demands not only temporal coherence of double the path length of the interferometer in single-ended mode, but also spatial coherence across the beam, which is sheared.

Corrections must be applied to the length measured in the double-ended mode to take account of the phase change at the surfaces of the bar and their roughnesses - this correction is larger than when the bar is wrung, since in the latter case the surfaces of the platen and the bar face the same direction and should have similar surface roughnesses and phase corrections and only the difference between the corrections for the two surfaces is used, whereas in the un-wrung case, their sum is used.

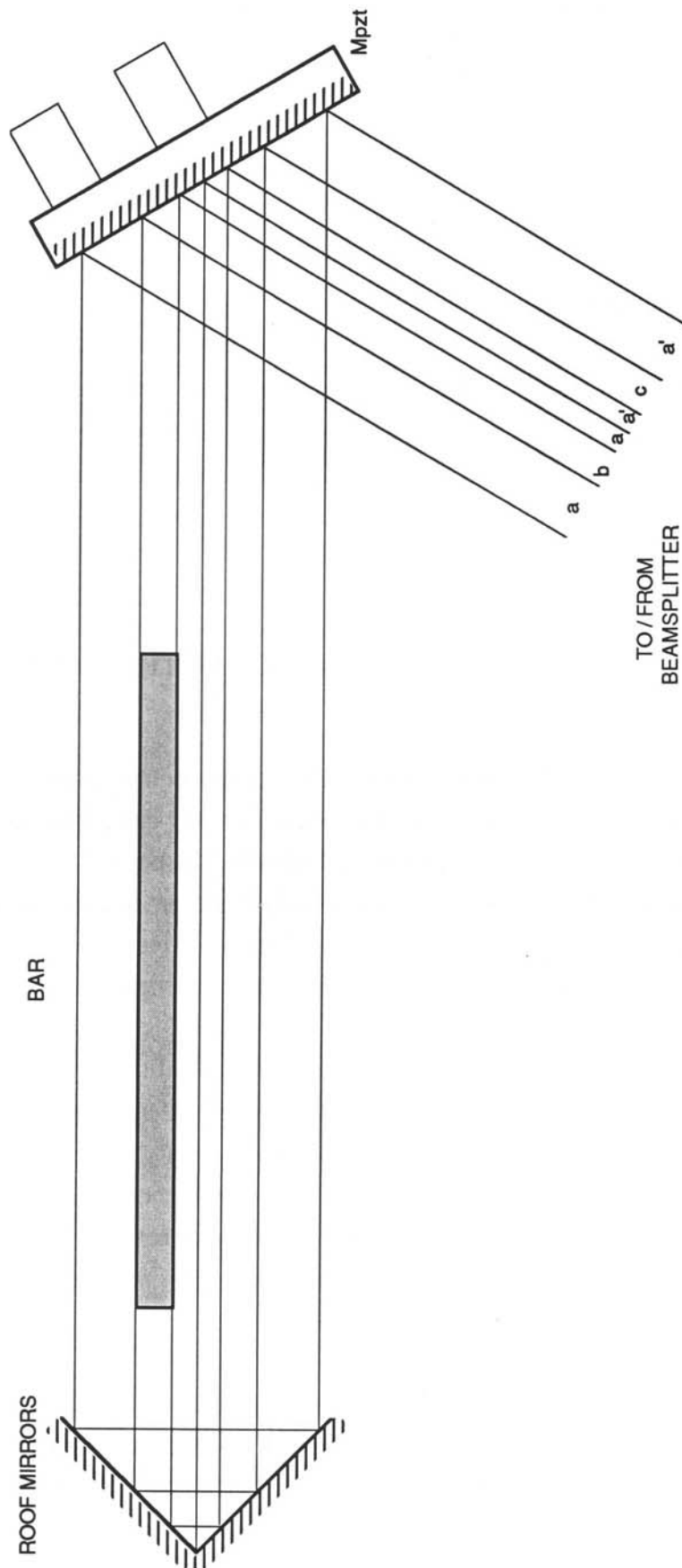


Figure 3.31 - Additional roof-mirror optics for double-ended interferometry

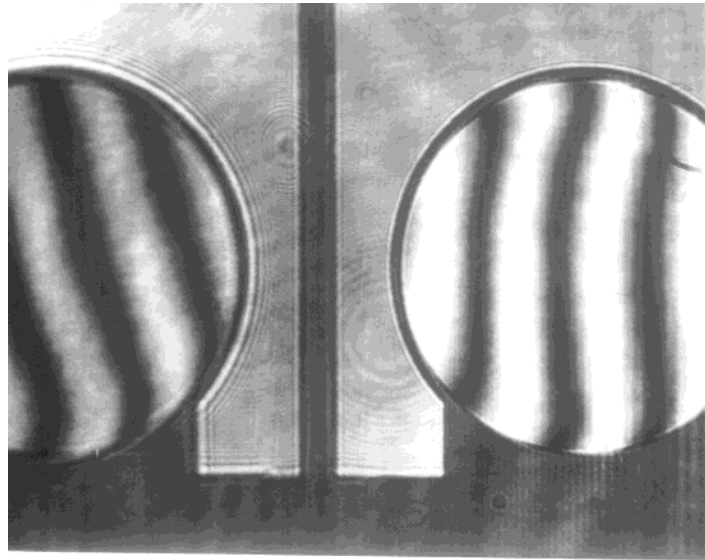


Figure 3.32 - Double ended image

3.5.1 Analysis of new double-ended interferometer

Re-arranging the optics into a linear design simplifies the analysis. The path length of the reference beam of the conventional Twyman-Green interferometer is included in the analysis to show that the interference is still between this reference beam and the beam in the measurement arm.

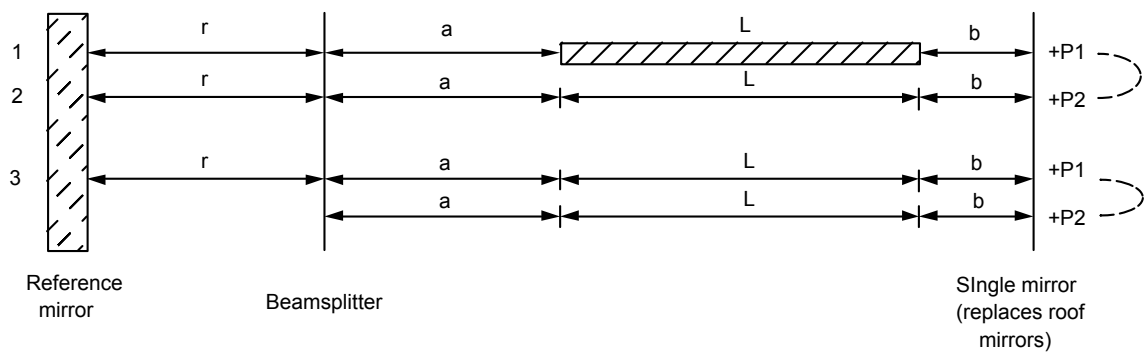


Figure 3.33 - Analysis of new double-ended interferometry

Representing the optical path distances by ϕ gives

$$\begin{aligned}
\phi_1 &= 2a - 2r \\
\phi_2 &= 2(a + L + 2b + P_1 + P_2) - 2r \\
\phi_3 &= 2a + 2L + 2b + P_1 + P_2 - 2r
\end{aligned} \tag{3.15}$$

Again, the two measured quantities are phase differences

$$\begin{aligned}
\phi_3 - \phi_1 &= 2L + 2b + P_1 + P_2 \\
\phi_3 - \phi_2 &= -2b - P_1 - P_2
\end{aligned} \tag{3.16}$$

and hence

$$(\phi_3 - \phi_1) + (\phi_3 - \phi_2) = 2L \tag{3.17}$$

As above, the factor of two is due to the double-pass nature of the design (as is the case for single-ended measurement) and means that the each fringe is half a wavelength in size. The effects of P_1 and P_2 , the phase changes at the mirror surfaces drop out of the analysis. Thus this system has the advantages outlined above, but uses fewer extra surfaces and is easier to align.

3.5.2 Double-ended phase-stepping

When the double-ended mirrors are adjusted correctly (see § 4.1.1.7), the fringes are straight and continuous across the join of the two mirrors. The fringes are adjusted to have the same tilt as for single-ended measurements (§ 4.1.5). The phase-stepping is performed as for single-ended measurements.

REFERENCES FOR CHAPTER 3

- [1] Lewis A J & Pugh D J Design Note: Interferometer light source and alignment aid using single-mode optical fibres *Meas. Sci. Technol.* **3** (1992) 929-930
- [2] CCDM 5th Session (1973) (*BIPM Sevres, France 92310*) M58
- [3] Jaseja T S, Javan A & Townes C H Frequency stability of He-Ne masers and measurements of length *Phys. Rev. Lett.* **10** (1963) 165-167
- [4] White A D A two-channel laser frequency control system *IEEE J. Quant. Elect.* **1** (1965) 322
- [5] Rowley W R C & Wilson D C Optical coupling effects in frequency stabilized lasers *Appl. Opt.* **11** (1972) 475-476
- [6] White A D, Gordon E I & Labuda E F Frequency stabilisation of single mode gas lasers *Appl. Phys. Lett.* **5** (1964) 97-98
- [7] Brillet A & Cérez P Laser frequency stabilization by saturated absorption *J. de Phys. (France)* **42 (C-8)** (1981) 73-82
- [8] Cérez P, Brillet A & Hartman F Metrological properties of the R(127) line of iodine studied by laser saturated absorption *IEEE Trans. Inst. Meas.* **IM-23** (1974) 526-528
- [9] Cérez P & Bennett S J Helium-neon laser stabilized by saturated absorption in iodine at 612 nm *Appl. Opt.* **18** (1979) 1079-1083
- [10] (Editor's Note) Documents concerning the new definition of the metre *Metrologia* **19** (1984) 163-177
- [11] Allan D W Statistics of atomic frequency standards *Proc. IEEE* **54** (1966) 221-230
- [12] Morris R H, Ferguson J B & Warmiac J S Frequency stabilization of internal mirror He-Ne lasers in a transverse magnetic field *Appl. Opt.* **14** (1975) 2808
- [13] Umeda N, Tsukiji M & Takasaki H Stabilized ^3He - ^{20}Ne transverse Zeeman laser *Appl. Opt.* **19** (1980) 442-450
- [14] Fellman T, Junger P & Stahlberg B Stabilisation of a green He-Ne laser *Appl. Opt.* **26** (1987) 2705-2706
- [15] Baer T, Kowalski F V & Hall J L Frequency stabilization of a 0.633 μm He-Ne longitudinal Zeeman laser *Appl. Opt.* **19** (1980) 3173-3177
- [16] Rowley W R C The performance of a longitudinal Zeeman-stabilised He-Ne laser (633 nm) with thermal modulation and control *Meas. Sci. Technol.* **1** (1990) 348-351
- [17] Tomlinson W J & Fork R L Properties of gaseous optical masers in weak axial magnetic fields *Phys. Rev.* **164** (1968) 480-483
- [18] Sasagawa G S & Zumberge M A Five year frequency stability of a Zeeman-stabilised laser *Appl. Opt.* **28** (1989) 824-825
- [19] Virdee M S *NPL Report MOM* **108** (1992) 1-16

- [20] Lowenthal S & Joyeux D Speckle removal by a slowly moving diffuser associated with a motionless diffuser *J. Opt. Soc. Am.* **61** (1971) 847-851
 - [21] Bowman M J Two new methods of improving optical image quality *Appl. Opt.* **7** (1968) 2280-2284
 - [22] Lewis A J & Pugh D J Design Note: Interferometer light source and alignment aid using single-mode optical fibres *Meas. Sci. Technol.* **3** (1992) 929-930
 - [23] Ai C & Wyant J C Effect of piezoelectric transducer nonlinearity on phase shift interferometry *Appl. Opt.* **26** (1987) 1112-1116
 - [24] Ohyama N, Kinoshita S, Corneso-Rodriguez A, Honda T & Tsujiuchi J Accuracy of phase determination with unequal reference phase shift *J. Opt.Soc. Am.* **5** (1988) 2014-2025
 - [25] Cheng YY & Wyant J C Phase shifter calibration in phase shifting interferometry *Appl. Opt.* **24** (1985) 3049-3052
 - [26] Schwider J Phase shifting interferometry: reference phase error reduction *Appl. Opt.* **28** (1989) 3889-3892
 - [27] Harb S, Smith S T & Chetwynd D G Subnanometre behaviour of a capacitive feedback piezoelectric displacement actuator *Rev. Sci. Instrum.* **63** (1992) 1680-1689
 - [28] Private communication, G Bönsch, PTB Germany
 - [29] Bennett J M Recent developments in surface roughness characterization *Meas. Sci. Technol.* **3** (1992) 1119-1127
 - [30] Ishikawa S, Bönsch G, & Böhme H Phase-shifting interferometry with a coupled interferometer: Application to optical roughness of gauge blocks *Optik* **91** (1992) 103-108
 - [31] Leach R K Investigation into the measurement of the wringing effect and the phase shift at reflection applied to the accurate measurement of end standards *MSc feasibility study*, Brunel University (1993)
 - [32] Kaye G W C & Laby T H *Tables of Physical and Chemical Constants* 15th edn (1989) (Harlow, Essex: Longmans)
 - [33] Saunders J B A high-sensitivity interferometer for measurement of phase-shift and other applications *NBS Circular* **581** (1957) 51-59
 - [34] Dorenwendt K Interferenteile Messung von nicht angeschobenen Endmaßen *PTB Annual Rep.* (1973) 121
-